
ALMA multiline observations toward the central region of NGC 613

Yusuke MIYAMOTO¹, Naomasa NAKAI^{2,3}, Masumichi SETA⁴, Dragan SALAK⁴, Makoto NAGAI² and Hiroyuki KANEKO¹

¹Nobeyama Radio Observatory, NAOJ, Nobeyama, Minamimaki, Minamisaku, Nagano 384-1305, Japan

²Division of Physics, Faculty of Pure and Applied Sciences, University of Tsukuba, Tsukuba, Ibaraki 305-8571, Japan

³Center for Integrated Research in Fundamental Science and Technology (CiRfSE), University of Tsukuba, Tsukuba, Ibaraki 305-8571, Japan

⁴Department of Physics, School of Science and Technology, Kwansai Gakuin University, 2-1 Gakuen, Sanda, Hyogo 669-1337, Japan

*E-mail: miyamoto.yusuke@nao.ac.jp

Received 2017 February 27; Accepted 2017 July 15

Abstract

We report ALMA observations of molecular gas and continuum emission in the 90 and 350 GHz bands toward a nearby Seyfert galaxy NGC 613. Radio continuum emissions were detected at 95 and 350 GHz from both the circum-nuclear disk (CND) ($r \lesssim 90$ pc) and a star-forming ring ($250 \text{ pc} \lesssim r \lesssim 340$ pc), and the 95 GHz continuum was observed to extend from the center at a position angle of $20^\circ \pm 8^\circ$. The archival 4.9 GHz data and our 95 GHz data show spectral indices of $\alpha \lesssim -0.6$ and -0.2 along the jets and in the star-forming ring; these can be produced by synchrotron emission and free-free emission, respectively. In addition, we detected the emission of CO(3-2), HCN(1-0), HCN(4-3), HCO⁺(1-0), HCO⁺(4-3), CS(2-1), and CS(7-6) in both the CND and ring. The rotational temperatures and column densities of molecules derived from $J = 1 - 0$ and $4 - 3$ lines of HCN and HCO⁺ and $J = 2 - 1$ and $7 - 6$ of CS in the CND and ring were derived. Furthermore, a non-LTE model revealed that the kinetic temperature of $T_k = 350\text{--}550$ K in the CND is higher than $T_k = 80\text{--}300$ K in the ring, utilizing the intensity ratios of HCN, HCO⁺, and CS. The star-formation efficiency in the CND is almost an order of magnitude lower than those at the spots in the star-forming ring, while the dominant activity of the central region is the star formation rather than active galactic nuclei. We determined that the large velocity dispersion of CO extending toward the north side of the CND and decomposing into blueshifted and redshifted features is probably explained by the effect of the radio jets. These results strongly suggest that the jets heat the gas in the CND, in which the feedback prevents star formation.

Key words: galaxies: individual (NGC 613) — galaxies: nuclei — galaxies: ISM — ISM: molecules — radio lines: galaxies — galaxies: active

1 Introduction

For understanding the activity and evolution of active galactic nuclei (AGN), it is essential to investigate its fueling process.

AGN must be fed with material available in the galactic disk of the host galaxy. The galactic bar can effectively drain angular momentum of interstellar gas and transport the gas inward to

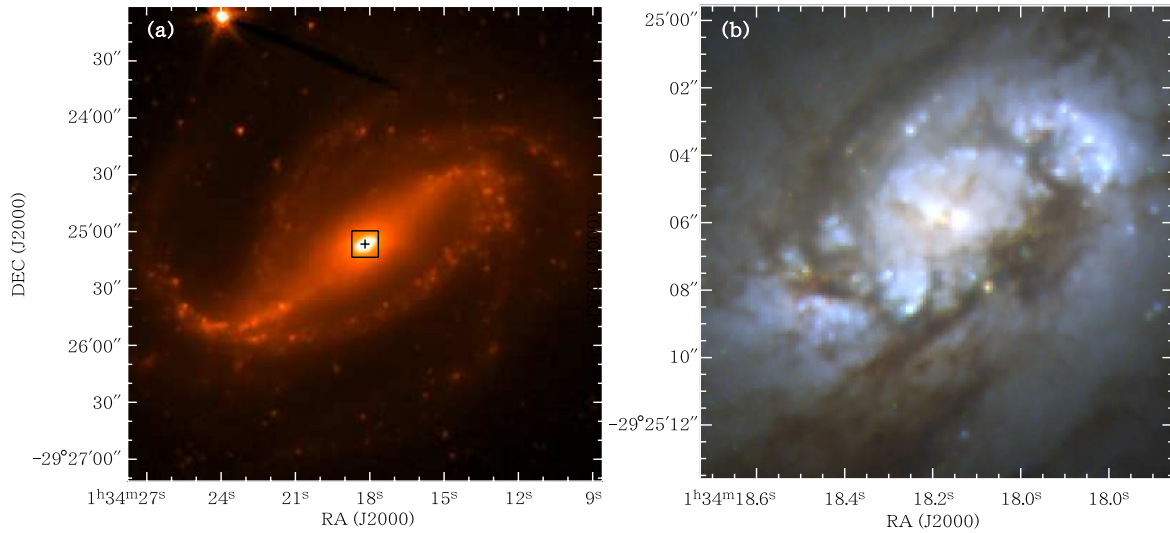


Fig. 1. (a) IRAC image of NGC 613 in $3.6 \mu\text{m}$ obtained from the Spitzer Survey of Stellar Structure in Galaxies ($S^4\text{G}$, Sheth et al. 2010). (b) HST WFPC2 image of the center region of NGC 613. The image region corresponds to the box in the IRAC image (left) and ALMA images in figures 2, 5, and 10 .

Table 1. Parameters of NGC 613

Parameter	Value	References	this work *
RA (J2000.0)	$1^{\text{h}}34^{\text{m}}18^{\text{s}}.235$	Skrutskie et al. 2006	$1^{\text{h}}34^{\text{m}}18^{\text{s}}.1901$
Dec (J2000.0)	$-29^{\circ}25'6''.56$		$-29^{\circ}25'6''.601$
Distance	17.5 Mpc	Tully 1988	—
Position angle	120°	de Vaucouleurs et al. 1991	118° (4°)
Inclination angle	41°	de Vaucouleurs et al. 1991	46° (1°)
Systemic velocity (LSR)	$1470 \pm 5 \text{ km s}^{-1}$	Koribalski et al. (2004)	1471 km s^{-1} (3 km s^{-1})

* Values in parentheses represent the uncertainties.

the disk center. The gas gathers on nearly circular orbits (x_2 orbits) and forms nuclear rings ($r \sim$ a few 100 pc) (Binney & Tremaine 1987). CO surveys have shown that central concentration of molecular gas is higher in barred galaxies than in non barred galaxies (e.g., Sakamoto et al. 1999, Nishiyama et al. 2001, Sheth et al. 2005). However, the rings as dynamical barriers can prevent the gas from flowing inward (Regan & Teuben 2004). This is supported by the result that a correlation cannot be determined between the galactic bars and AGN activities (Hunt & Malkan 1999). To discuss the fueling process of AGN, we must investigate the dynamics and physical properties of molecular gas from the ring to the center via the circum-nuclear disk (CND) at $r \sim 1\text{--}100$ pc.

X-ray radiation and jet/outflow are important feedbacks of the AGN. X-ray radiation from AGN can effectively heat gas in the nuclear region because it can penetrate large amounts of dust and gas. Therefore, the X-ray radiation generates internal turbulence in the CND and constricts mass accretion to the center (Wada 2012). Such an X-ray dominated region (XDR; e.g., Maloney et al. 1996, Meijerink & Spaans 2005) can contribute to the enhancement of several molecular lines; for example, HCN and its physical properties have been estimated through multiline observations of dense gas tracers (e.g., Krips et al. 2008, Krips et al. 2011). However, recent multi-

line observations have suggested that the enhancement is explained by high-temperature chemistry (e.g., mechanical heating) rather than XDR chemistry (e.g., Izumi et al. 2013, Martín et al. 2015, Izumi et al. 2016). Jet/outflow activities from AGNs can also heavily influence the fueling process in the CND and ring. Recent observations toward the center of NGC 1068 with high spatial resolution (\sim several 10 pc, e.g., Krips et al. 2011, García-Burillo et al. 2014, Viti et al. 2014) showed that the HCN distribution, which traces a dense gas of $n(\text{H}_2) \gtrsim 10^4 \text{ cm}^{-3}$, is concentrated at the center. In addition, the molecular outflow signatures from the AGN were identified not only in the CO but also in the HCN and HCO^+ . The jet can drag gas outwards on scales of ~ 100 pc, and hence regulate activity of the accretion disk (Combes et al. 2013). In addition, note that shock heating by the jet is an important heating source that generates turbulence. It is necessary to derive the physical properties, such as temperature and density of shocked gas in the CND, to identify the heating source of the hot gas in the CND.

The nearby barred galaxy NGC 613 (figure 1) hosts a low-luminosity AGN, which is identified through mid infrared spectroscopy (Goulding & Alexander 2009) and X-ray observations by using the XMM-Newton (Castangia et al. 2013). NGC 613 is one of the best targets for studying the jet/outflow activities due to the proximity (17.5 Mpc; Tully 1988), relatively abundant

Table 2. Observational log with ALMA

Band	Array	Observation Date	Bandpass calibrator	Flux calibrator	Phase calibrator	Observation time (on source)
3	7 m × 9	2014 June 5	J0137-2430	Uranus	J0145-2733	18 min
	12 m × 31	2014 December 5	J0334-4008	Uranus	J0145-2733	6 min
	12 m × 35	2015 April 25	J2357-5311	Uranus	J0145-2733	5 min
	12 m × 43	2015 July 3	J0334-4008	Neptune	J0145-2733	10 min
	TP	2015 September 3	–	–	–	29 min
	TP	2015 September 19	–	–	–	61 min
7	7 m × 10	2014 June 8	J0137-2430	Uranus	J0145-2733	13 min
	7 m × 10	2015 June 6	J0238+1636	Uranus	J0137-2430	12 min
	7 m × 12	2015 June 8	J2253+1608	Uranus	J0137-2430	13 min
	12 m × 33	2014 June 14	J0137-2430	J0334-401	J0145-2733	7 min
	12 m × 39	2015 June 3	J2232+1143	Ceres	J0145-2733	7 min
	TP	2015 August 28	–	–	–	71 min

Table 3. Observational parameters of lines

Band	Molecule	Transition	Frequency (GHz) ^a	E_u/k (K) ^b	Beam size (″)
3	SiO	$J=2-1$	86.846995	6.25	0″.73×0″.64 ($P.A. = 68^\circ$)
	HCN	$J=1-0$	88.631847	4.25	0″.72×0″.63 ($P.A. = 68^\circ$)
	HCO ⁺	$J=1-0$	89.188526	4.28	0″.72×0″.63 ($P.A. = 68^\circ$)
	CS	$J=2-1$	97.980953	7.05	0″.67×0″.58 ($P.A. = 68^\circ$)
7	CS	$J=7-6$	342.882857	65.83	0″.37×0″.31 ($P.A. = 83^\circ$)
	CO	$J=3-2$	345.79599	33.19	0″.44×0″.37 ($P.A. = 45^\circ$)
	HCN	$J=4-3$	354.505473	42.53	0″.43×0″.37 ($P.A. = 40^\circ$)
	HCO ⁺	$J=4-3$	356.734242	42.80	0″.36×0″.29 ($P.A. = 84^\circ$)

^a adopted from NIST Recommended Rest Frequencies for Observed Interstellar Molecular Microwave Transitions (F. J. Lovas et al.; <http://physics.nist.gov/cgi-bin/micro/table5/start.pl>) ^b Leiden Atomic and Molecular Database (LAMDA: Schöier et al. 2005)

molecular gas around the center (e.g., Elfhag et al. 1996), activity shown by the radio jet (Hummel et al. 1987), and nuclear ring with moderate inclination ($i \sim 55^\circ$, Hummel & Jorsater 1992). The basic parameters of NGC 613 are summarized in table 1. The nuclear ring, which is clearly defined in Br γ , is likely to be disturbed at the north-east by the outflow from the AGN. The high flux ratio of [FeII]-to-Br γ and large velocity dispersion of [FeII] support the interaction between the outflow and nuclear ring (Falcón-Barroso et al. 2014). In contrast, the high flux of H₂ in the center can be explained by the heating due to the X-ray radiation or/and shock (e.g., Maloney et al. 1996, Hollenbach & McKee 1989).

In this paper, we present Atacama large millimeter/submillimeter array (ALMA) cycle 2 observations toward the central region of NGC 613 at Bands 3 and 7. The remainder of this paper is structured as follows. Section 2 describes the observations and data reduction. In section 3, the distribution of continuum and molecular gas is presented, and the basic parameters of NGC 613 are determined. The physical conditions of the molecular gas in the central region both under local

thermodynamic equilibrium (LTE) and non-LTE conditions are investigated and the activities for explaining the gas heating at the CNB are discussed in section 4. Finally, conclusions are drawn in section 5.

2 Observations

NGC 613 was observed through the ALMA using Bands 3 and 7 receivers, as a Cycle 2 early science program (ID 2013.1.01329.S, PI: Miyamoto). For both Bands 3 and 7 observations, the 12-m array, Atacama compact array (ACA) and total power array (TP) were used. The baseline lengths extended up to 1573.0 m (524.3 k λ at 100 GHz) for Band 3 and 780.7 m (923.9 k λ at 355 GHz) for Band 7. The typical synthesized beams at Bands 3 and 7 were 0″.7 and 0″.4, corresponding to 59 and 34 pc, respectively, at the distance of the galaxy. Single-point observations were conducted using the 12-m array and ACA for Band 3 and three-point mosaic observations were conducted using the 12-m array and ACA for Band 7. These setups allowed us to image a CNB of ~ 100 pc diameter and the sur-

rounding star-forming ring of ~ 600 pc diameter (Böker et al. 2008; Falcón-Barroso et al. 2014). The phase reference center was adopted to be $(\alpha_{J2000.0}, \delta_{J2000.0}) = (1^{\text{h}}34^{\text{m}}18^{\text{s}}.235, -29^{\circ}25'06''.56)$ (Skrutskie et al. 2006). Observations at Band 3 were conducted from June 2014 to September 2015. The correlators for Band 3 were configured to set three spectral windows in the lower sideband to cover SiO(2–1) ($\nu_{\text{rest}} = 86.846960$ GHz), HCN(1–0) ($\nu_{\text{rest}} = 88.631601$ GHz), and $\text{HCO}^+(1-0)$ ($\nu_{\text{rest}} = 89.188526$ GHz) and two in the upper sideband to measure CS(2–1) ($\nu_{\text{rest}} = 97.980953$ GHz) and 100 GHz continuum, both in the 2SB dual-polarization mode. Observations at Band 7 were conducted from June 2014 to August 2015. The correlators for Band 7 were configured to set two spectral windows in the lower sideband to cover CO(3–2) ($\nu_{\text{rest}} = 345.795990$ GHz) and CS(7–6) ($\nu_{\text{rest}} = 342.882857$ GHz) and two in the upper sideband to measure HCN(4–3) ($\nu_{\text{rest}} = 354.505473$ GHz) and $\text{HCO}^+(4-3)$ ($\nu_{\text{rest}} = 356.734242$ GHz), both in the dual-polarization mode. Table 2 summarizes the observational logs for this project. Note that we could only cover the CO(3–2) line with $V_{\text{LSR}} = 1250$ – 1660 km s $^{-1}$ because of spectral setting restrictions, while CO(1–0) observations with SEST, whose angular resolution was $44''$, revealed that the CO(1–0) velocity range was $V_{\text{LSR}} \sim 1250$ – 1710 km s $^{-1}$ (Elfhag et al. 1996). The proportion of the CO(1–0) intensity at $V_{\text{LSR}} = 1250$ – 1660 km s $^{-1}$ to the total intensity at $V_{\text{LSR}} = 1250$ – 1710 km s $^{-1}$ is $\sim 97\%$, and the equivalent underestimation of the total flux can be expected in CO(3–2).

The data were processed using the Common Astronomy Software Application (CASA; McMullin et al. 2007). The velocity resolution of each line data obtained at different observing tracks with the 12 m array and ACA were separately rearranged to be 10 km s $^{-1}$, except for the resolution of 2.5 km s $^{-1}$ in CO(3–2). Each line data was then combined after subtracting continuum emission determined at the emission-free channels. To image the continuum emission, we used the flux density at the emission-free channels. The imaging was performed using the CLEAN-algorithm in CASA. CLEAN maps were obtained considering the Briggs weighting mode on the data with a robustness of 0.5. The resultant maps were 1500×1500 pixels with $0''.05$ per pixel. For the line emission images, TP data were calibrated through flagging and the system temperature correction, and imaged independently from the 12-m array and ACA data. By using the Feather algorithm in CASA, the low-resolution image obtained through the TP and high-resolution image obtained through the 12-m and ACA were converted into the gridded visibility plane and combined. Finally, the data was reconverted into a combined image. The synthesized beams of CO(4–3), $\theta = 0''.37 \times 0''.31$ ($P.A. = 82^\circ$), and of HCN(4–3), $\theta = 0''.36 \times 0''.30$ ($P.A. = 84^\circ$) with the 12-m array and ACA change to $\theta = 0''.44 \times 0''.37$ ($P.A. = 45^\circ$) and

$\theta = 0''.43 \times 0''.37$ ($P.A. = 40^\circ$), respectively, after applying the Feather-algorithm. The observational parameters of each line are given in table 3.

3 Results

3.1 Continuum emission

Figures 2 (a) and (b) respectively show the 95 and 350 GHz continuum maps toward the central $14''$ (1.2 kpc) region of NGC 613. Continuum emission was detected from both the CNB ($r \lesssim 90$ pc) and the star-forming ring ($250 \text{ pc} \lesssim r \lesssim 340 \text{ pc}$) (section 3.3.2). The flux of 95 GHz continuum in the central region ($r \leq 6''$) with only the 12-m array (9.79 ± 0.06 mJy) is comparable to that with the 12-m array and ACA (10.02 ± 0.06 mJy), indicating that the continuum emission is dominated by compact sources. We fit a two-dimensional Gaussian to the nuclear 350 GHz continuum source to derive the position and intrinsic size of the nucleus by using imfit in CASA. The source size deconvolved from the synthesized beam of $0''.39 \times 0''.29$ ($P.A. = 84^\circ$) is $0''.230 \times 0''.186$ ($P.A. = 147^\circ$), corresponding to 19.5×15.8 pc at the distance of 17.5 Mpc. The position of the peak flux of the 350 GHz continuum (2.180 ± 0.085 mJy beam $^{-1}$) is at $(\alpha_{J2000.0}, \delta_{J2000.0}) = (1^{\text{h}}34^{\text{m}}18^{\text{s}}.901, -29^{\circ}25'06''.601)$ with an uncertainty of $0''.02$, which is consistent with the positions of the optical nucleus (Hummel et al. 1987) and an ultraluminous X-ray point source (Liu & Bregman 2005). Hereafter, we adopt the peak position as the center of NGC 613.

The 95-GHz continuum elongates from the center at a position angle of $20^\circ \pm 8^\circ$, which is consistent with that of low-frequency radio continuum of 4.9 and 14.9 GHz within the error ($P.A. = 12^\circ$, Hummel & Jorsater 1992). We obtained the 4.9 GHz data (project AH231) from Very Large Array (VLA) archives and reanalyzed them in a standard manner in CASA. Figure 2(d) shows the 4.9-GHz continuum image with a resolution of $0''.8 \times 0''.8$. Figure 2(e) shows the distribution of the spectral index (α) between 4.9 and 95 GHz; it is convolved with a resolution of $0''.8$ [figure 2(c)]. At the center, the spectral index $\alpha \sim -0.6$. The index is slightly flatter than that derived from 4.9 and 14.9 GHz continuum images (-0.8 ; Hummel & Jorsater 1992), suggesting the contribution of free-free emission from H II regions in addition to synchrotron emission (e.g., Condon 1992). The same spectral index of $\alpha \sim -0.7$ at 4.9–14.9 and 4.9–95 GHz at the southern blob $0''.9$ from the center implies that the blob can be dominated by synchrotron emission due to the nuclear jets (Hummel et al. 1987). In contrast, the flat spectrum ($\alpha \sim -0.2$) in the ring can be produced through the free-free emission from young star-formation regions (Falcón-Barroso et al. 2014).

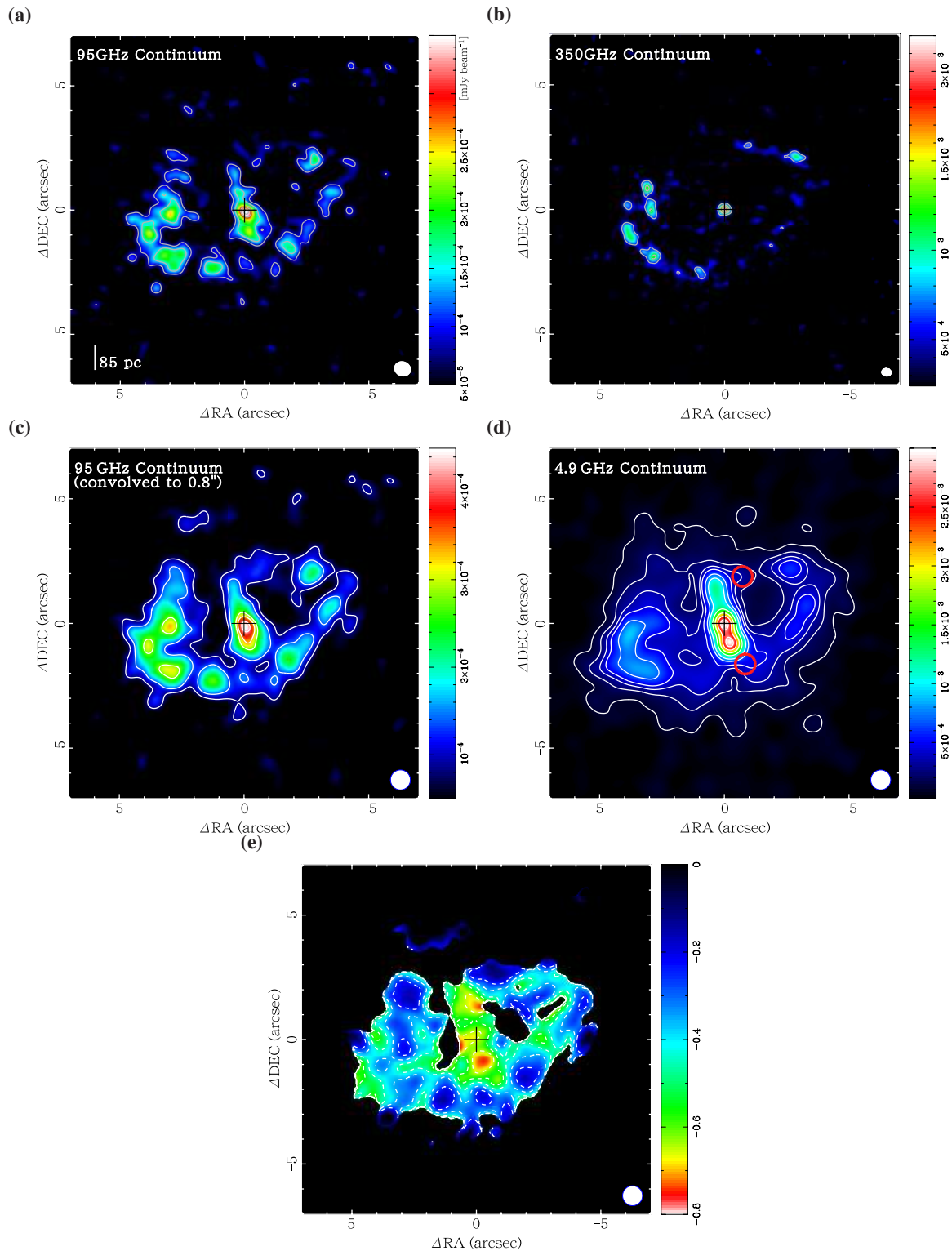


Fig. 2. (a) 95 GHz continuum map with a resolution of $0.''64 \times 0.''56$ ($PA = 68^\circ$). The contour levels are 3σ , 5σ , 10σ , and 12σ , where $1\sigma = 30 \mu\text{Jy beam}^{-1}$. (b) 350 GHz continuum map with a resolution of $0.''39 \times 0.''29$ ($PA = 84^\circ$). The contour levels are 5σ , 10σ , and 15σ , where $1\sigma = 0.12 \text{ mJy beam}^{-1}$. (c) Same as panel (a) but convolved to $\theta = 0.''8$. The contour levels are 3σ , 5σ , 10σ , 12σ , and 15σ , where $1\sigma = 28 \mu\text{Jy beam}^{-1}$. (d) The 4.9 GHz continuum map with a resolution of $0.''8 \times 0.''8$. The contour levels are 5σ , 10σ , 15σ , 20σ , 30σ , 40σ , 60σ , 80σ , 100σ , and 120σ , where $1\sigma = 23 \mu\text{Jy beam}^{-1}$. SiO is detected in positions shown in circles. (e) Spectral index distribution calculated from 4.9 GHz (above 2σ) and 95 GHz (above 2σ). The contour levels are spectral indices of -0.15 , -0.35 , -0.45 , -0.55 , and -0.65 .

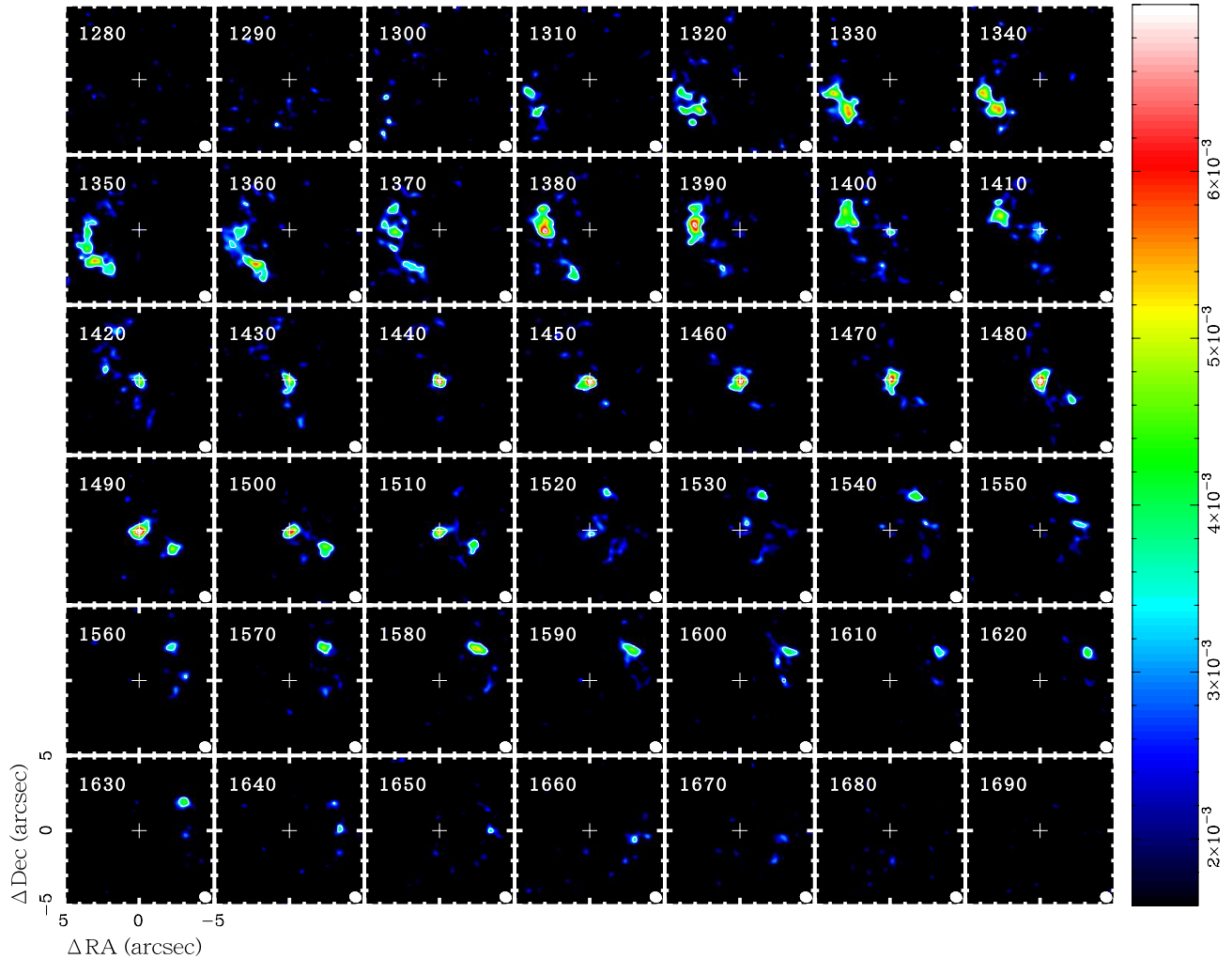


Fig. 3. Channel maps of $\text{HCO}^+(1-0)$ emission in the central $10'' \times 10''$ region, corresponding to 848×848 pc at the distance of the galaxy (17.5 Mpc). The channels have an interval of 10 km s^{-1} , and the central velocities are labeled at the upper left corner. The synthesized beam of $0''.72 \times 0''.63$ ($P.A. = 68^\circ$) is shown at the right bottom corner. Crosses show the position of the galactic center. Contours levels are 4σ and 8σ , where $1\sigma = 0.8 \text{ mJy beam}^{-1}$.

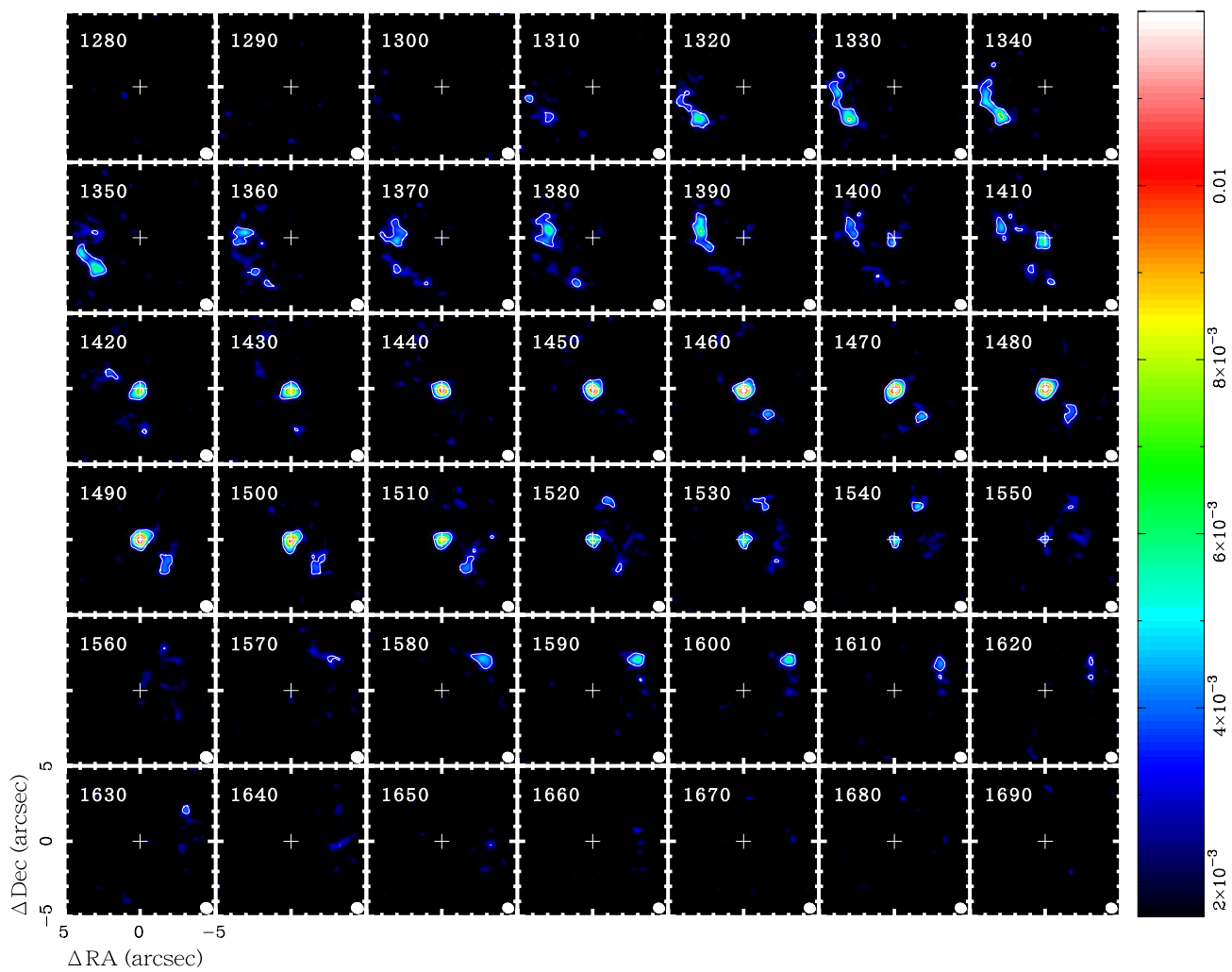


Fig. 4. Same as figure 3, but for HCN (1–0) emission. Contours levels are 4σ , 8σ , and 12σ , where $1\sigma = 0.8 \text{ mJy beam}^{-1}$.

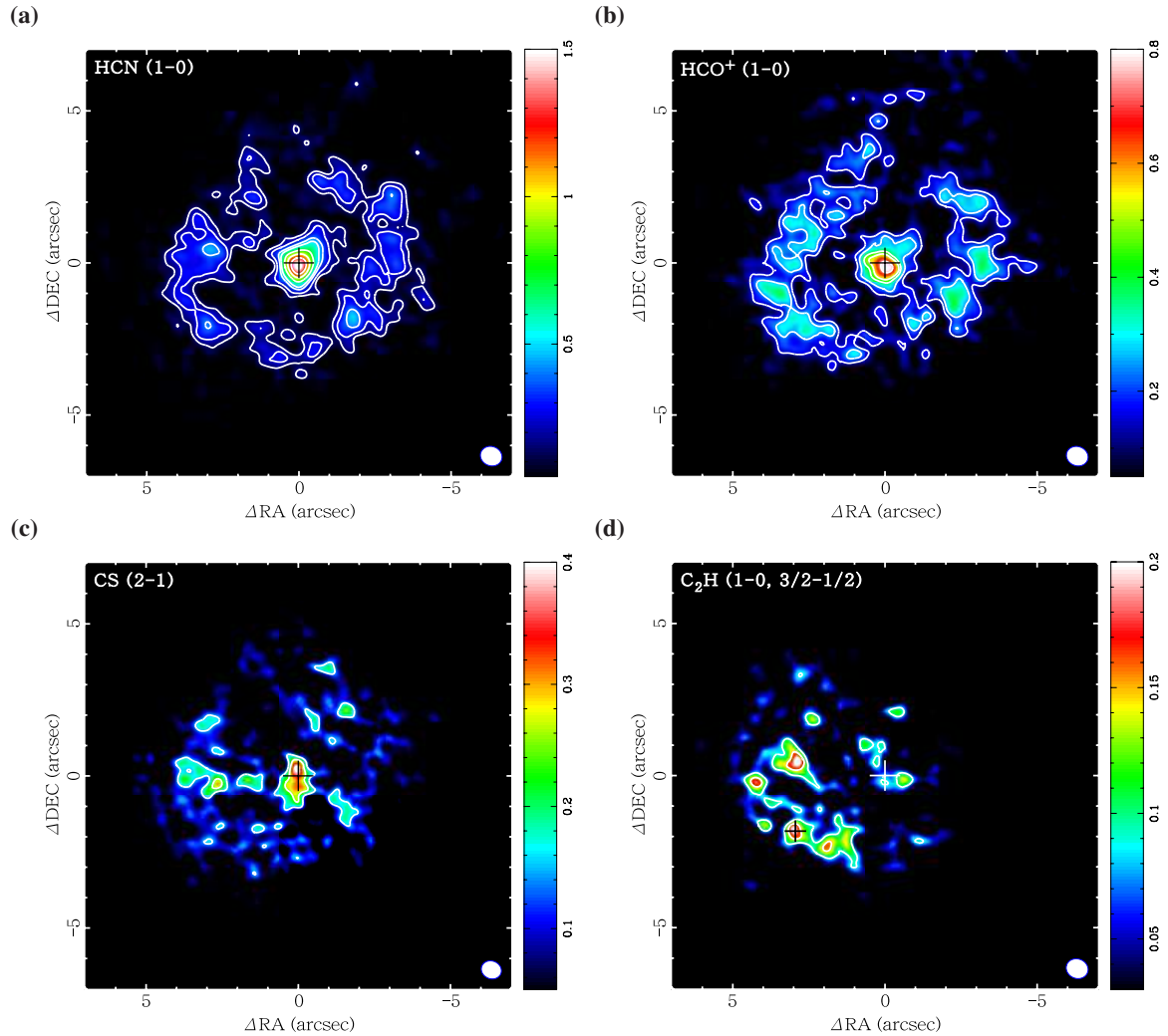


Fig. 5. Integrated intensity maps of (a) HCN(1-0), (b) HCO⁺(1-0), (c) CS(2-1), and (d) C₂H(1-0, 3/2-1/2) in the central 14'' × 14''. The synthesized beams are shown at the right bottom corner and the positions of the galactic center is represented by crosses. The contours are (a) 3, 5, 8, 10, 15, 20, 25, and 30 σ where $1\sigma = 0.05 \text{ Jy km s}^{-1}$; (b) 3, 5, 8, 10, and 15 σ where $1\sigma = 0.05 \text{ Jy km s}^{-1}$; (c) 3, 5, and 8 σ where $1\sigma = 0.05 \text{ Jy km s}^{-1}$; and (d) 3 and 5 σ where $1\sigma = 0.03 \text{ Jy km s}^{-1}$.

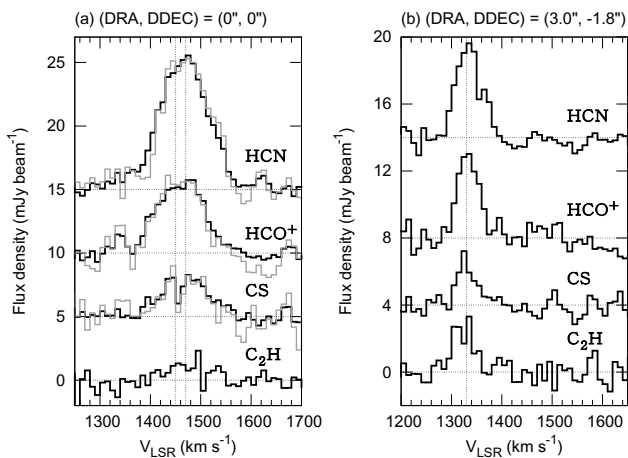


Fig. 6. $C_2H(1-0, 3/2-1/2)$, $CS(2-1)$, $HCO^+(1-0)$, and $HCN(1-0)$ spectra at (a) the dynamical center $(\Delta\alpha, \Delta\delta) = (0'', 0'')$, and (b) position shown by the black cross in figure 5(d), $(\Delta\alpha, \Delta\delta) = (3''.0, -1''.8)$. The gray lines in (a) are spectra derived from only the 12-m extended array, providing the angular resolution of $0.60 \times 0''.52$, $0.60 \times 0''.51$, and $0.56 \times 0''.46$ for HCN , HCO^+ , and CS , respectively. The vertical lines in (a) and (b) correspond to the velocity region of the CS dip ($V_{LSR} = 1450-1470 \text{ km s}^{-1}$) and velocity of peak intensity of HCN ($V_{LSR} = 1330 \text{ km s}^{-1}$), respectively.

3.2 Molecular gas distribution

3.2.1 Band3

Figures 3 and 4 respectively show the channel maps of $HCO^+(1-0)$ and $HCN(1-0)$ line emissions from the central $10'' \times 10''$ region of NGC 613, in which these lines were detected in the same velocity range of $1310-1660 \text{ km s}^{-1}$. Figures 5 (a)–(c) show the intensity maps of $HCN(1-0)$, $HCO^+(1-0)$, and $CS(2-1)$, respectively, integrated over a velocity range of $1150-1750 \text{ km s}^{-1}$, where emission-free channels were masked to derive the integrated intensities of the weak emission accurately and enhance the contrasts. $HCN(1-0)$, $HCO^+(1-0)$, and $CS(2-1)$ lines were detected from both the CND and star-forming ring. We determined that intensities of HCN and HCO^+ show peaks toward the center but a dip of CS with $\gtrsim 4\sigma$ [see figure 6 (a)]. The dip occurs at a velocity of the peak temperature of $CS(7-6)$ ($V_{LSR} \sim 1460 \text{ km s}^{-1}$, figure 11). Recent observations have reported self and/or continuum absorption lines in dense gas tracers, e.g., HCN , HCO^+ , and CS toward the nuclei of Seyfert galaxies and (ultra) luminous infrared galaxies ((U)LIRGs) (e.g., Aalto et al. 2015, Scoville et al. 2015, Martín et al. 2016, Lin et al. 2016). Although the absorption of HCN and HCO^+ toward the center of NGC 613 cannot be identified from the combined data of all arrays ($\theta \sim 0''.7$) apparently (black lines in figure 6), by using only the 12-m extended array ($\theta \sim 0''.6$), we can recognize the dip features (or plateau) at the velocity of $V_{LSR} \sim 1460 \text{ km s}^{-1}$ (gray lines in figure 6). These results indicate that the size of the absorbing cloud is significantly smaller than the beam size ($\theta \sim 0.5'' = 42 \text{ pc}$).

We also detected $C_2H(1-0, 3/2-1/2)$ line at 87.316925 GHz

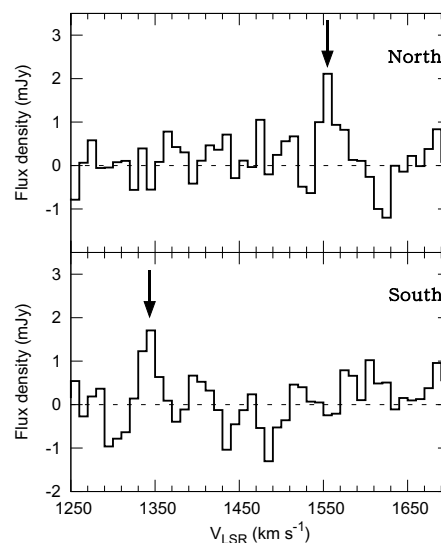


Fig. 7. Top and bottom panels show $SiO(2-1)$ spectra detected at the regions indicated by the northern and southern circles in figure 2 (d), respectively.

at the east side of the ring [figure 5 (d)]. The detection of C_2H line was confirmed by similar features of $HCN(1-0)$, $HCO^+(1-0)$, and $CS(2-1)$ spectra [figure 6 (b)] at a peak position of C_2H represented by a circle in figure 5 (d). It has been reported that C_2H is produced in the UV irradiated cloud edges associated with massive star-forming regions (Beuther et al. 2008; Meier & Turner 2005). From $Br\gamma$ observations of the central region of NGC 613, Falcón-Barroso et al. (2014) derived star-formation rates of $0.10-0.13 M_\odot \text{ yr}^{-1}$ at some spots in the east side of the ring; these were clearly higher than those in the west, $0.03-0.06 M_\odot \text{ yr}^{-1}$. In addition, we found peaks of C_2H located close to those of $CO(3-2)$ [figure 10 (a)]. These results indicate that C_2H traces the photodissociation region in the ring, thus being consistent with the result of NGC 1097 (Martín et al. 2015). However, $SiO(2-1)$, known as a tracer of shocks (e.g., Martín-Pintado et al. 1992), is detected marginally [signal-to-noise ratio (S/N) ~ 4 ; figure 7] at the edge of the radio jets, as shown by circles in figure 2 (d), probably indicating the existence of shock regions related to the jets. However, for a detailed discussion, it is necessary to improve data quality.

3.2.2 Band7

Figures 8 and 9 show the channel maps of the $HCO^+(4-3)$ and $HCN(4-3)$ line emissions, respectively, from the central $10'' \times 10''$ region of NGC 613. As the critical densities of $J = 4-3$ transitions of HCO^+ and HCN ($n_{H_2}^{crit} \sim 10^{6-7} \text{ cm}^{-3}$) are several orders of magnitude higher than those of $J = 1-0$ ($n_{H_2}^{crit} \sim 10^{4-5} \text{ cm}^{-3}$), the distribution of the higher transitions is much compact than those of the lower transitions, and the $HCO^+(4-3)$ and $HCN(4-3)$ emissions at the west side of the star-forming ring are weaker than those at the east side where

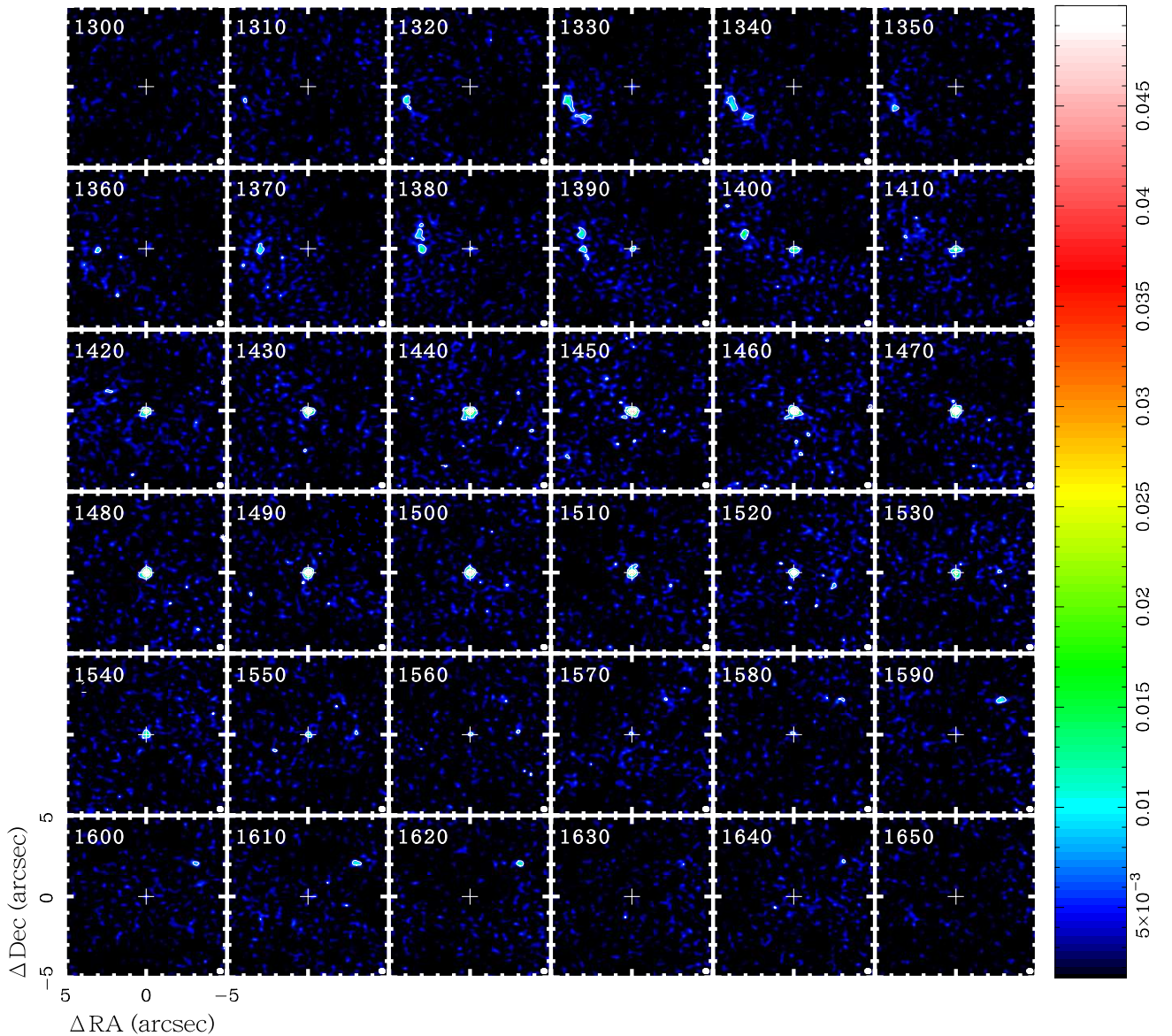


Fig. 8. Channel maps of $\text{HCO}^+(4-3)$ emission in the central $10'' \times 10''$ region, corresponding to 848×848 pc at the distance of the galaxy (17.5 Mpc). The channels have an interval of 10 km s^{-1} and the central velocities are labeled at the upper left corner. The synthesized beam of $0''.36 \times 0''.29$ ($P.A. = 84^\circ$) is shown at the right bottom corner. Crosses show the position of the dynamical center. Contours levels are 4σ , 10σ , 15σ , 20σ and 25σ where $1\sigma = 1.5 \text{ mJy beam}^{-1}$.

star formation is active (Falc3n–Barroso et al. 2014).

Figures 10 (a)–(d) show the velocity-integrated intensity maps in the same manner as Band 3 but the velocity range of $1250\text{--}1660 \text{ km s}^{-1}$ for $\text{CO}(3-2)$ and $1250\text{--}1650 \text{ km s}^{-1}$ for $\text{HCN}(4-3)$. The high velocity components of $\text{HCN}(4-3)$ ($V_{\text{LSR}} \gtrsim 1630 \text{ km s}^{-1}$) are regarded as negligible (figure 9). $\text{HCN}(4-3)$, $\text{HCO}^+(4-3)$, and $\text{CS}(7-6)$ were detected in the CND and a part of the star-forming ring. In contrast, $\text{CO}(3-2)$ was detected in the CND and star-forming ring and along the galactic bar. The southern galactic bar is weaker than the northern; this may be attributed to the limited high velocity range of $\text{CO}(3-2)$.

3.3 Basic parameters of NGC 613

3.3.1 Systemic velocity, position angle, inclination angle, and rotation curve

Figure 11 shows the spectra of $\text{CO}(3-2)$, $\text{CS}(7-6)$, $\text{HCN}(4-3)$, and $\text{HCO}^+(4-3)$ toward the center of NGC 613, $(\alpha_{\text{J2000.0}}, \delta_{\text{J2000.0}}) = (1^{\text{h}}34^{\text{m}}18^{\text{s}}.190, -29^{\circ}25^{\text{m}}06^{\text{s}}.60)$. By fitting the Gaussian to these line profiles, we derived the central velocity of $V_{\text{LSR}} = 1471.3 \pm 0.3 \text{ km s}^{-1}$, which was consistent with the systemic velocity determined by Koribalski et al. (2004), that is, $V_{\text{sys}} = 1470 \pm 5 \text{ km s}^{-1}$ in radio definition with respect to LSR.

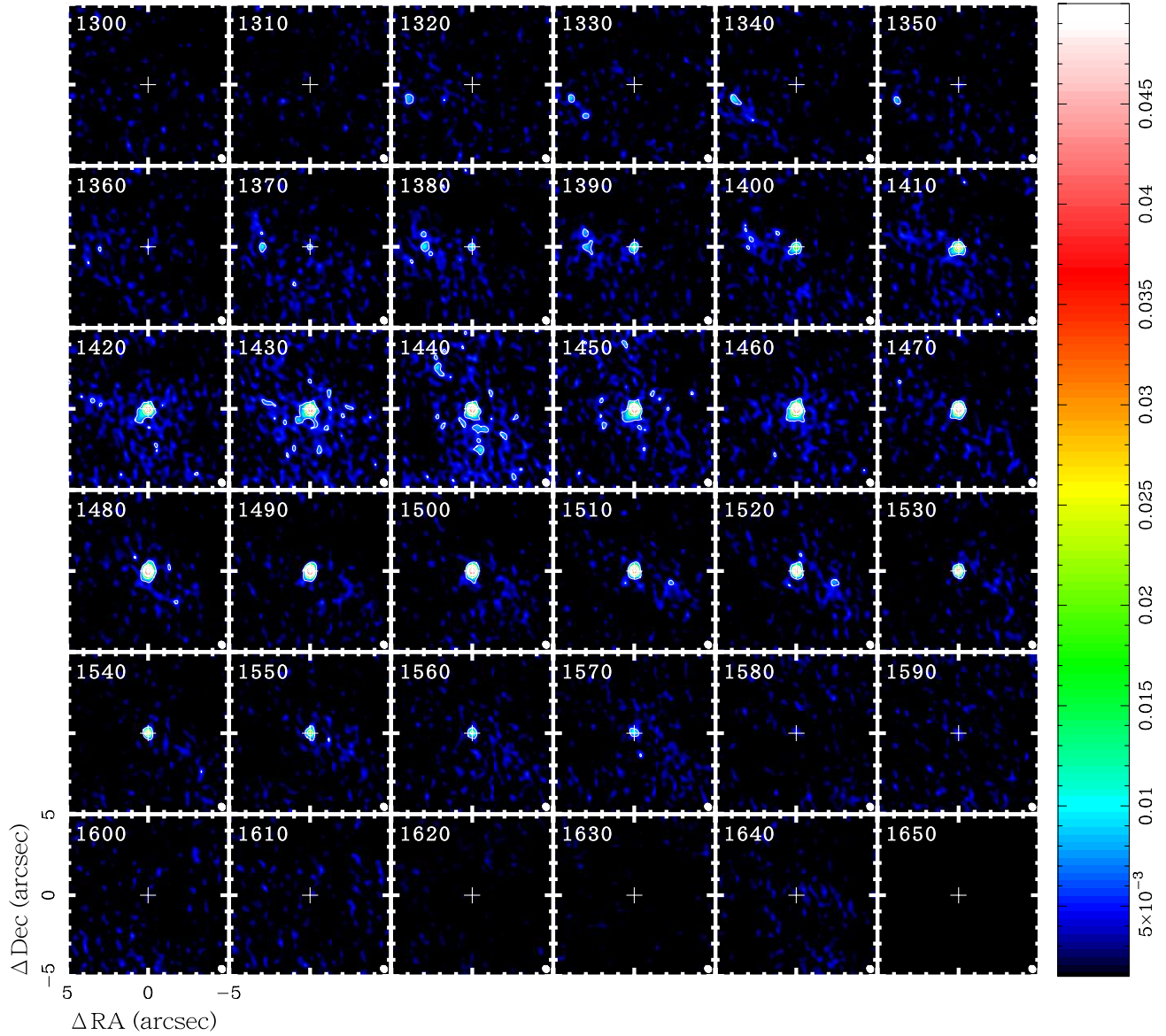


Fig. 9. Channel maps of HCN(4–3) emission in the central $10'' \times 10''$ region, corresponding to 848×848 pc at the distance of the galaxy (17.5 Mpc). The channels have an interval of 10 km s^{-1} , and the central velocities are labeled at the upper left corner. The synthesized beam of $0''.43 \times 0''.37$ ($P.A. = 40^\circ$) is shown at the right bottom corner. Crosses show the position of the dynamical center. Contours levels are 4σ , 10σ , 15σ , 20σ , and 25σ , where $1\sigma = 1.7 \text{ mJy beam}^{-1}$.

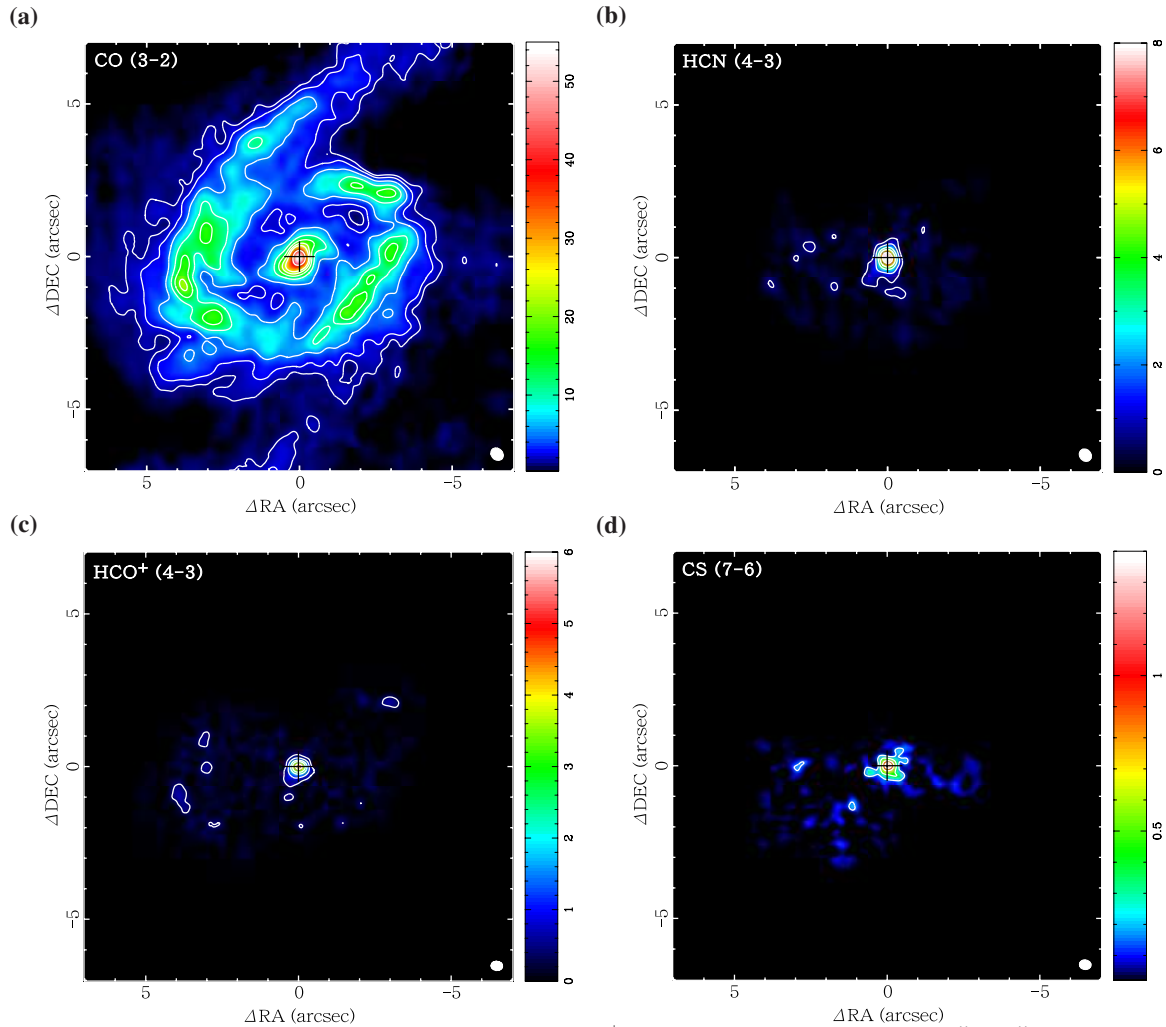


Fig. 10. Integrated intensity maps of (a) CO(3–2), (b) HCN(4–3), (c) HCO⁺(4–3), and (d) CS(7–6) in the central 14'' × 14''. The synthesized beams are shown at the right bottom corner, and the positions of the galactic center shown by crosses. The contours are (a) 3, 5, 10, 20, 30, 40, 50, 80, and 110 σ , where 1 σ = 0.5 Jy km s^{−1}; (b) 4, 10, 20, 30, 50, 70, and 80 σ , where 1 σ = 0.1 Jy km s^{−1}; (c) 4, 10, 20, 30, and 50 σ , where 1 σ = 0.1 Jy km s^{−1}, and (d) 4 σ where 1 σ = 0.03 Jy km s^{−1}.

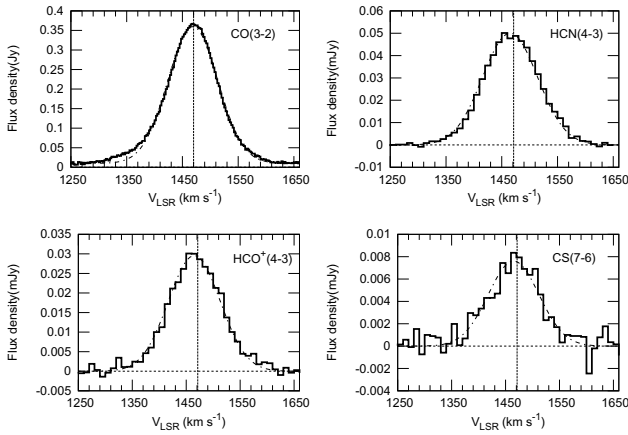


Fig. 11. CO(3–2), CS(7–6), HCN(4–3), and HCO⁺(4–3) emission line profiles toward the center of NGC 613. The corresponding aperture is 0[′].5 (42.4 pc). Gaussian fits to the lines are overlaid with the broken lines. The vertical dot lines are the central velocities of $V_{\text{LSR}} = 1471 \text{ km s}^{-1}$, derived from the Gaussian fitting to the spectra.

We kinematically determined the basic parameters of NGC 613, such as the systemic velocity (V_{sys}), inclination angle (i), position angle of the major axis (θ_{maj}), rotational velocity (V_{rot}), and velocity dispersion (v_s), by using the program of 3D-based analysis of rotating objects from line observations (^{3D}Barolo) that fits a 3D tilted-ring to spectroscopic data cubes (Di Teodoro & Fraternali 2015). The ^{3D}Barolo can estimate the basic parameters, such as the dynamical center (x_0, y_0), V_{sys} , i , θ_{maj} , V_{rot} , and v_s , by comparing the model with the observed data at each ring of radius r and width w , assuming that the ring has a constant circular velocity (V_{rot}) depending only on r . The data cube of CO(3–2) with the velocity resolution $\Delta v = 2.5 \text{ km s}^{-1}$ was utilized for this procedure. The central region of NGC 613 ($r \leq 5''$) was divided into 25 annuli with a width of $\Delta r = 0''.2 \sim \theta_{\text{maj}}/2$, where θ_{maj} is the synthesized beam size along its major axis, centered on the galactic center. The scale-height of the disk is estimated as $h_z = v_s^2/2\pi G\Sigma_{\text{H}_2}$, where v_s is the gas velocity dispersion, G is the gravitational constant, and Σ_{H_2} is the molecular gas surface density (section 3.3.2). For $v_s = 25 \text{ km s}^{-1}$ and $\Sigma_{\text{H}_2} = 200 M_{\odot} \text{ pc}^{-2}$ in the ring, the scale height $h_z \approx 150 \text{ pc}$. By adopting the dynamical center of NGC 613 ($\alpha_{\text{J2000.0}}, \delta_{\text{J2000.0}} = (1^{\text{h}}34^{\text{m}}18^{\text{s}}.190, -29^{\circ}25^{\text{m}}06^{\text{s}}.60)$) and scale-height $h_z = 150 \text{ pc}$, we derived V_{sys} , θ_{maj} , i , V_{rot} , and v_s as functions of the radius by ^{3D}Barolo. In all the fitting steps, we applied a weighting function of $|\cos\theta|$, where $\theta = 0$ corresponds to the major axis of the galaxy (X), to minimize the error caused by the points close to the minor axis (Y). The resultant V_{sys} of $1471 \pm 3 \text{ km s}^{-1}$ is consistent with the central velocities of CO(3–2), CS(7–6), HCN(4–3), and HCO⁺(4–3) spectra, and therefore we regarded $V_{\text{sys}} = 1471 \text{ km s}^{-1}$ as the systemic velocity of the galaxy.

Figure 12(a) shows the results of θ_{maj} and i derived through

this method. The position and inclination angles in the outer region than at $r \approx 4''.5$ change abruptly because of low S/N of the data. In addition, the values at the innermost region ($r < 0''.1$) cannot be determined rigidly because the size is smaller than that of the beam. For simplicity, $\theta_{\text{maj}} = 118^{\circ} \pm 4^{\circ}$ and $i = 46^{\circ} \pm 1^{\circ}$, which are mean values between the radii $r = 0''.2$ and $4''.5$, are regarded as the position and inclination angles, although the systematic radial variances of these angles can be due to the warp or misalignment between the CND and ring. The position and inclination angles are consistent with the result of de Vaucouleurs et al. (1991) ($\theta_{\text{maj}} = 120^{\circ}$) and the value of $i = 47^{\circ}$ adopted by Burbidge et al. (1964), respectively.

For the fixed values of $\theta_{\text{maj}} = 118^{\circ}$ and $i = 46^{\circ}$, the rotation velocity and velocity dispersion were derived (figure 12(b)). The velocity dispersion of $v_s \approx 50 \text{ km s}^{-1}$ at the CND decreases to $v_s \approx 20 \text{ km s}^{-1}$ with the radius and then increases to $v_s \approx 25 \text{ km s}^{-1}$ at the ring ($r \sim 3'' - 4''$). The rotation curve shows the rigid rotation as a function of $V_{\text{rot}} = 49 \pm 1 \text{ [km s}^{-1} \text{ arcsec}^{-1]} \times r$ at $r > 0''.5$, while the position–velocity diagram along the major axis shows that the velocity rises steeply in the central region ($r < 0''.5 \approx 42 \text{ pc}$; figure 13). It is difficult to derive the high-rotation velocity separately from the velocity dispersion because of the limited beam width of $0''.44 \times 0''.37$ for the Briggs weighting with a robustness of 0.5 [figure 13(a)] and even for the uniform weighting [$0''.32 \times 0''.28$; figure 13(b)]. To resolve the degeneracy and clarify the variance of the rotation velocity, observations with higher angular resolutions would be needed. If the rotational velocity is $V_{\text{rot}} = 100 \text{ [km s}^{-1}] \sin(46^{\circ})$ at $r = 0''.1 (= 8.5 \text{ pc})$, the central dynamical mass becomes $M = 3.8 \times 10^7 M_{\odot}$, which is comparable to the supermassive black hole mass of NGC 613 ($\sim 10^7 M_{\odot}$) estimated by Beifiori et al. (2012) and Davis et al. (2014).

The red contours superimposed on the PV diagram by the data cube of CO(3–2) (black contour) in figure 13 are the best fit model with ^{3D}Barolo along $\theta_{\text{maj}} = 118^{\circ}$ (major axis) and $\theta_{\text{min}} = 28^{\circ}$ (minor axis) for $i = 46^{\circ}$. The model can trace the ring at $|X| \sim 3'' - 5''$ but not the high-velocity components in the CND at $|X| < 0''.5$. In the PV diagram along the minor axis, a bridging feature is observed between the CND and the southern part of the ring [$Y \sim (-1''.0) - (-2''.3)$]. Considering that the gas motion in NGC 613 is counterclockwise and the southern part of NGC 613 is on the near side (Burbidge et al. 1964), the components with a higher velocity than V_{sys} at $Y \sim 1'' - 2''$ may be associated with the outflow from the CND. The velocity shifts of $v > V_{\text{sys}}$ ($Y \sim -1''$) and $v < V_{\text{sys}}$ ($Y \sim -2''$) indicate the inflowing and outflowing gas, respectively, whereas it is difficult to explain this velocity shift based on the coplanar gas motion in the galactic disk. At the point of the velocity shift ($Y \sim -1''.5$), any particular gas distribution cannot be found (figure 10(a)); however, the point corresponds to

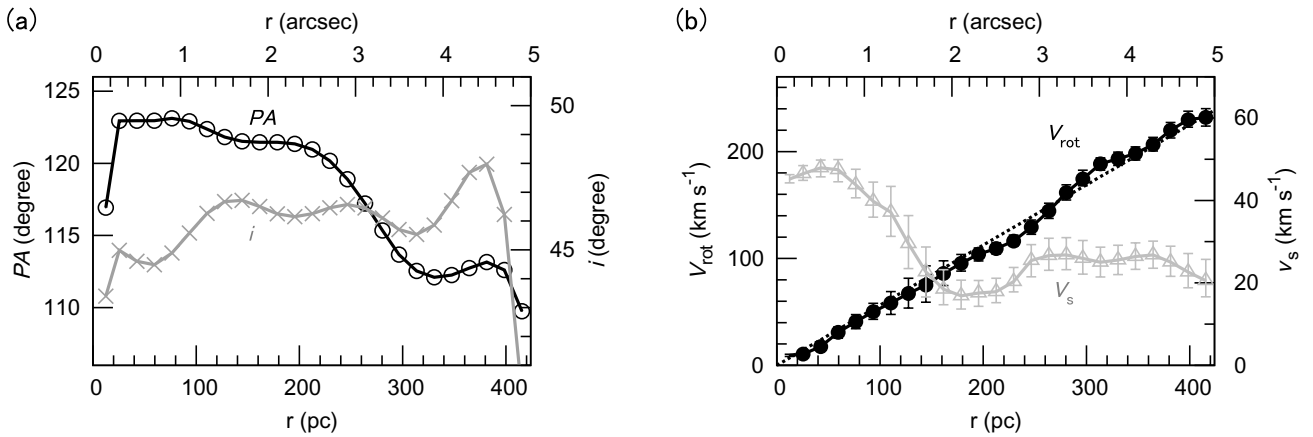


Fig. 12. Radial variation of (left) the position angle of the major axis, inclination angle, (right) rotational velocity, and velocity dispersion of the central region of NGC 613 ($r \leq 5''$). These values were kinematically determined using ^{3D}Barolo (Di Teodoro & Fraternali 2015).

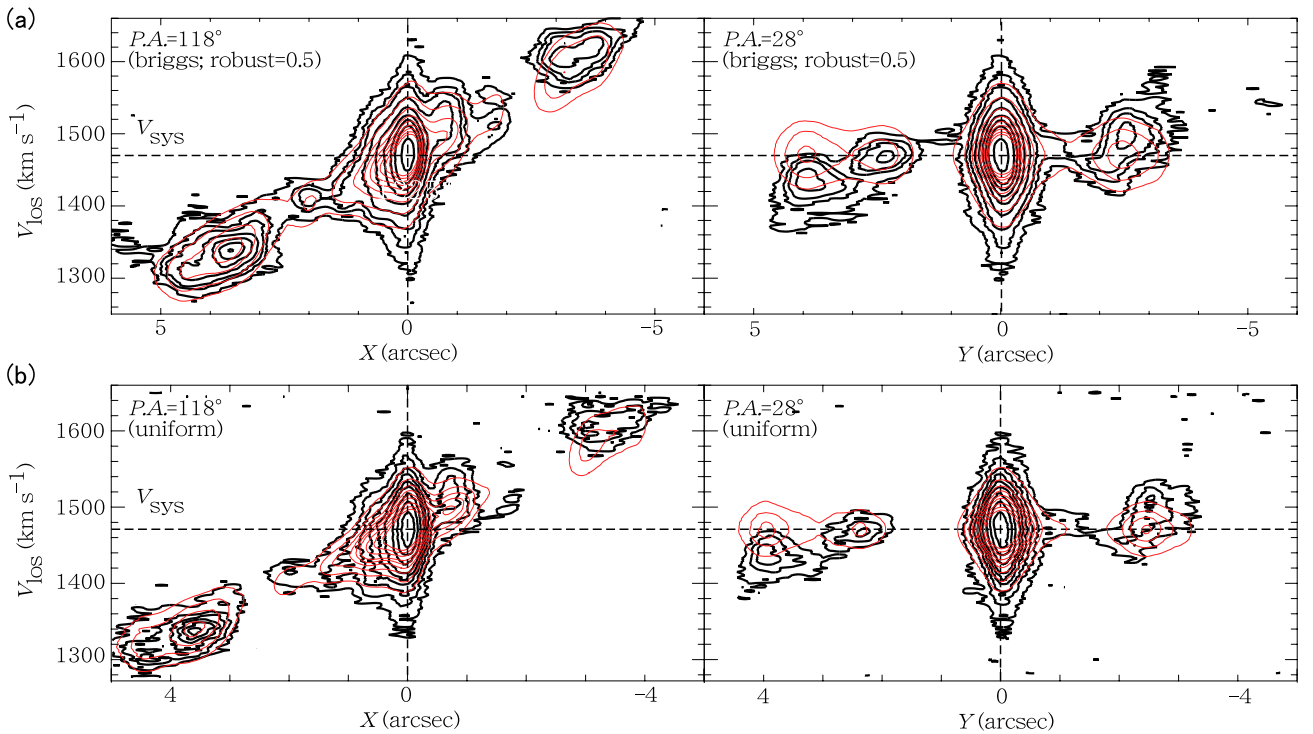


Fig. 13. (a) PV diagrams of CO(3–2) along the major axis (X) $P.A. = 118^\circ$ and minor axis (Y) $P.A. = 28^\circ$ for the Briggs weighting with a robustness of 0.5 in CLEAN. Contour levels are 0.02, 0.04, 0.06, 0.1, 0.15, 0.2, 0.25, 0.3, and 0.4 Jy beam⁻¹. Red contours show the PV diagram of best fits model obtained using ^{3D}Barolo. (b) Same as panel (a) but for the uniform weighting in CLEAN ($\theta_{\text{FWHM}} = 0''.33 \times 0''.29$). Contour levels are 0.025, 0.05, 0.075, 0.1, 0.125, 0.15, 0.2, 0.25, and 0.3 Jy beam⁻¹.

the edge of the radio jets (figure 2(d)). In addition, an extent of strong [FeII] emission was reported from the center to around the velocity shift point (Falc3n-Barroso et al. 2014). The velocity shift is presumed to diffuse outflowing gas over a wide-range direction such as a spherical bubble (e.g., Wagner & Bicknell 2011). The velocity offset ($v > V_{\text{sys}}$) at the outer ring ($|Y| \gtrsim 2''.5$) is caused by the noncircular (inflow) motion of the galactic bar because the velocity difference from systemic velocity ($\Delta V \sim 30 \text{ km s}^{-1}$) is obviously larger than the effect

of the uncertainty of the inclination ($\Delta = \pm 1^\circ$) on the rotation velocity ($\sim 6\% \approx 7 \text{ km s}^{-1}$).

3.3.2 Mass and radial distribution of molecular gas

Figure 14 shows the spectra of CO(3–2) with ALMA TP array and of CO(1–0) with SEST for comparison (Elfhag et al. 1996). The integrated intensities of CO(3–2) over the velocity range of 1280–1680 km s⁻¹ within the beam of $\theta_{\text{FWHM}} = 44''$ and $22''$ are $I_{\text{CO}32} = 8.5 \pm 0.4$ and $31.2 \pm 0.9 \text{ K km s}^{-1}$, re-

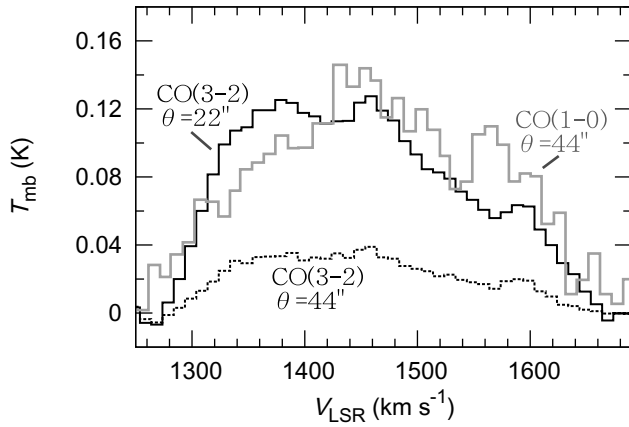


Fig. 14. Comparison among the spectra of CO(3–2) with ALMA TP array and CO(1–0) with SEST (gray, Elfhag et al. 1996) toward the central region of NGC 613. The spectra of CO(3–2) are convolved with the beam of $\theta_{\text{FWHM}}=44''$ (black dash) and $22''$ (black solid).

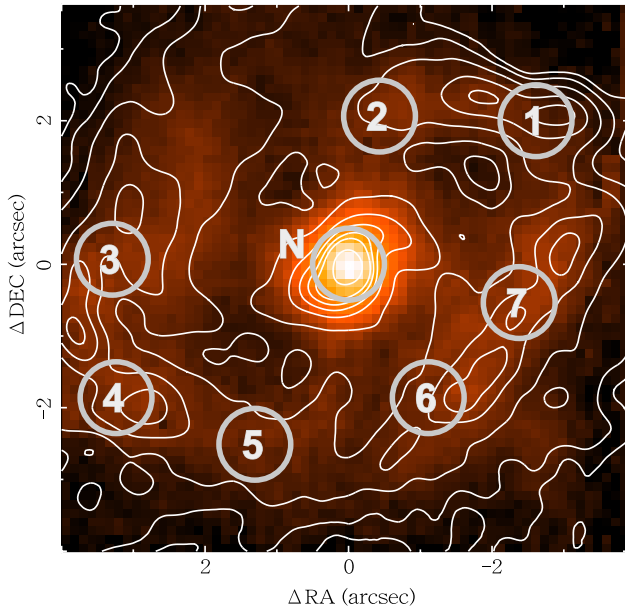


Fig. 15. VLT H_2 map (color; Falc3n–Barroso et al. 2014) overlaid with contours of CO(3–2) integrated intensity (figure 10(a)). The peak positions of these maps matched each other. The circles mark the positions of the nucleus and spots 1 through 7 denoted by Falc3n–Barroso et al. (2014).

spectively, and that of CO(1–0) with $\theta_{\text{FWHM}} = 44''$ is $I_{\text{CO}10} = 33.7 \pm 0.8 \text{ K km s}^{-1}$. For the same beam size ($\theta_{\text{FWHM}} = 44''$) in both CO(1–0) and CO(3–2), the ratio of CO(3–2) to CO(1–0) is $R_{32/10} = 0.25 \pm 0.01$, which is consistent with the values of $R_{32/10} = 0.2\text{--}0.7$ toward the centers of 28 nearby galaxies observed through a beamwidth of $21''$ (Mauersberger et al. 1999). However, for the central region of $r \leq 5''$ ($=420 \text{ pc}$), the $R_{32/10}$ could be underestimated because it increases toward the center (e.g., Dumke et al. 2001, Muraoka et al. 2007, Tsai et al. 2012, Vlahakis et al. 2013, Garc3a–Burillo et al. 2014). Matsushita et al. (2004) showed $R_{32/10} \geq 1.9 \pm 0.2$ at the nucleus of the Seyfert 2 galaxy M51, whose IR luminosity in

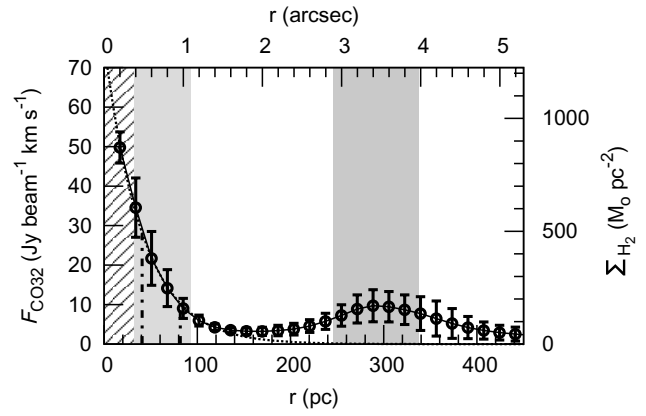


Fig. 16. The solid line presents the radial distribution of CO(3–2) emission of NGC 613. The CO-integrated intensities are azimuthally averaged with the correction for the inclination of 46° . The right-hand axis shows the surface densities for $R_{32/10} = 2$ calculated using equation (2). The dotted line presents a fitted exponential profile of $\Sigma_{\text{H}_2} = 1330 \exp(-r/r_e) [M_\odot \text{ pc}^{-2}]$ ($r_e = 41 \text{ pc}$), at $r \leq 100 \text{ pc}$. The vertical broken lines show the radii r_e and $2r_e$. The diagonal hatched region ($r \leq 0.75r_e$), light gray region ($0.75r_e \leq r \leq 2.25r_e$), and dark gray region ($6r_e \leq r \leq 8.25r_e$) are defined as the inner CND, outer CND, and star-forming ring, respectively.

$8\text{--}1000 \mu\text{m}$ comparable to that of NGC 613 (Sanders et al. 2003), averaged over the beamsize of $4''.2 \times 3''.4$. The intensity ratio of M51 ($R_{32/10} = 0.8 \pm 0.1$) derived from $I_{\text{CO}10} = 53.4 \pm 4.3 \text{ K km}^{-1}$ over $\theta_{\text{FWHM}} = 44''$ (Young et al. 1995) and $I_{\text{CO}32} = 44.4 \pm 2.8 \text{ K km}^{-1}$ over $\theta_{\text{FWHM}} = 22''$ (Mao et al. 2010) is slightly smaller than the intensity ratio of NGC 613 ($R_{32/10} = 0.93 \pm 0.03$) using CO(1–0) over $\theta_{\text{FWHM}} = 44''$ and CO(3–2) over $\theta_{\text{FWHM}} = 22''$, although the distance of M51 ($\sim 8.4 \text{ Mpc}$; Feldmeier et al. 1997) is approximately a half that of NGC 613. We adopted the $R_{32/10} \sim 2$ as the upper limit in the central region of NGC 613 ($r \leq 5''$). The molecular mass of $3.0 \times 10^8 M_\odot$ in the central region of NGC 613 ($r \leq 22''$) can be derived from the CO(1–0) intensity of $I_{\text{CO}} = 33.7 \text{ K km s}^{-1}$ by adopting the CO-to- H_2 conversion factor of $X_{\text{CO}} = 0.5 \times 10^{20} \text{ cm}^{-2} (\text{K km s}^{-1})^{-1}$ (Bolatto et al. 2013). The total flux within the region of $r \leq 5''$ is $S_{\text{CO}32} = 2.15 \times 10^3 \text{ Jy km s}^{-1}$, which corresponds to $M_{\text{H}_2} = 7.2 \times 10^7 \text{--}5.8 \times 10^8 M_\odot$, given by (e.g., Kohno et al. 2002, Bolatto et al. 2013)

$$\left(\frac{M_{\text{H}_2}}{M_\odot}\right) = 2.2 \times 10^2 \frac{1}{R_{32/10}} \left(\frac{\lambda}{0.87 \text{ mm}}\right)^2 \left(\frac{S_{\text{CO}32}}{\text{Jy km s}^{-1}}\right) \times \left(\frac{D}{\text{Mpc}}\right)^2 \left[\frac{X_{\text{CO}}}{0.5 \times 10^{20} \text{ cm}^{-2} (\text{K km s}^{-1})^{-1}}\right] \quad (1)$$

for $R_{32/10} = 0.25\text{--}2$ with galaxy distance $D = 17.5 \text{ Mpc}$.

By using the integrated intensity of CO(3–2) ($F_{\text{CO}32}$), galaxy inclination i , beamwidths θ_{maj} and θ_{min} , and conversion factor X_{CO} , the face-on surface density of molecular gas is given by

$$\left(\frac{\Sigma_{\text{H}_2}}{M_\odot \text{ pc}^{-2}}\right) = 8.2 \cos i \frac{1}{R_{32/10}} \left(\frac{\lambda}{0.87 \text{ mm}}\right)^2 \left(\frac{\theta_{\text{maj}}}{\text{arcsec}}\right)^{-1}$$

$$\begin{aligned} & \times \left(\frac{\theta_{\min}}{\text{arcsec}} \right)^{-1} \left(\frac{F_{\text{CO}32}}{\text{Jy beam}^{-1} \text{ km s}^{-1}} \right) \\ & \times \left[\frac{X_{\text{CO}}}{0.5 \times 10^{20} \text{ cm}^{-2} (\text{K km s}^{-1})^{-1}} \right]. \quad (2) \end{aligned}$$

Figure 16 shows the radial distribution of Σ_{H_2} for $R_{32/10} = 2$, which was derived by averaging into annuli with width of $0''.2$ ($= 17$ pc). Position angle $PA = 118^\circ$ and inclination angle $i = 46^\circ$ were adopted as the parameters of the ellipses. The radial distribution Σ_{H_2} shows an exponential decrease (dotted line) of $\Sigma_{\text{H}_2} = 1330 \exp(-r/r_e) [M_\odot \text{ pc}^{-2}]$, where $r_e = 0''.48 (= 41 \text{ pc})$ at $r \leq 100 \text{ pc}$. We define the regions $r \leq 0''.36 (= 0.75r_e)$, $0''.36 (= 0.75r_e) \leq r \leq 1''.08 (= 2.25r_e)$, and $2''.88 (= 6r_e) \leq r \leq 3''.96 (= 8.25r_e)$ as the inner CN, outer CN, and star-forming ring, respectively.

4 Discussion

4.1 LTE analysis

The rotational temperatures (T_{rot}) and column densities (N_{mol}) of HCN, HCO^+ , and CS can be estimated from the rotational diagrams, assuming optically thin LTE. The rotational diagram is the logarithmic plot of the normalized column densities with the statistical weight of the level as a function of energy levels corresponding to the transitions (cf. Izumi et al. 2013). To construct the rotational diagram of each observed molecule, i.e., HCN, HCO^+ , and CS, the complete data in Bands 3 and 7 were convolved to the beam size of $0''.72 \times 0''.72$. As described in figure 16, we divided the central region of NGC 613 into three regions: the inner CN ($r \leq 0''.36$), outer CN ($0''.36 \leq r \leq 1''.08$), and star-forming ring ($2''.88 \leq r \leq 3''.96$). The resultant diagrams of HCN, HCO^+ , and CS are shown in figure 17, and the derived rotational temperatures and column densities of the molecules in the inner and outer CNs and in the star-forming ring are summarized in table 4. While the rotational temperatures and column densities of all molecules gradually decrease with the distance from the nucleus, the temperature of CS is slightly higher than those of HCN and HCO^+ (bottom-right panel of figure 17). Considering that the temperature of CS is high not only in the inner CN but also in the outer region, the absorption of CS(2–1) in the CN (figure 6) does not play a major role in the temperature. Note that T_{rot} and N were derived by fitting only two transitions with approximately one order of magnitude energy differences. By utilizing three transition lines ($J = 1-0$, $3-2$, and $4-3$) of HCN and HCO^+ , Izumi et al. (2013) suggested the presence of two temperature gas components in the CN of NGC 1097: one is responsible for the low- J ($J \leq 3$) emission and the other for the high- J ($J \geq 3$) emission. In addition, observations toward the center of nearby galaxies in multiple transitions of CS by using a single dish have presented the existence of two temperature gas components (e.g., Bayet et al. 2009, Aladro et al. 2011).

CS(7–6), whose energy level is higher than those of HCN(4–3) and $\text{HCO}^+(4-3)$, may trace the higher temperature components selectively. To examine the presence of two temperature components and the effect of the warm gas on the higher rotational temperature of CS, it is necessary to obtain the data of adjoining transitions.

4.2 The HCN/ HCO^+ and HCN/CS ratios

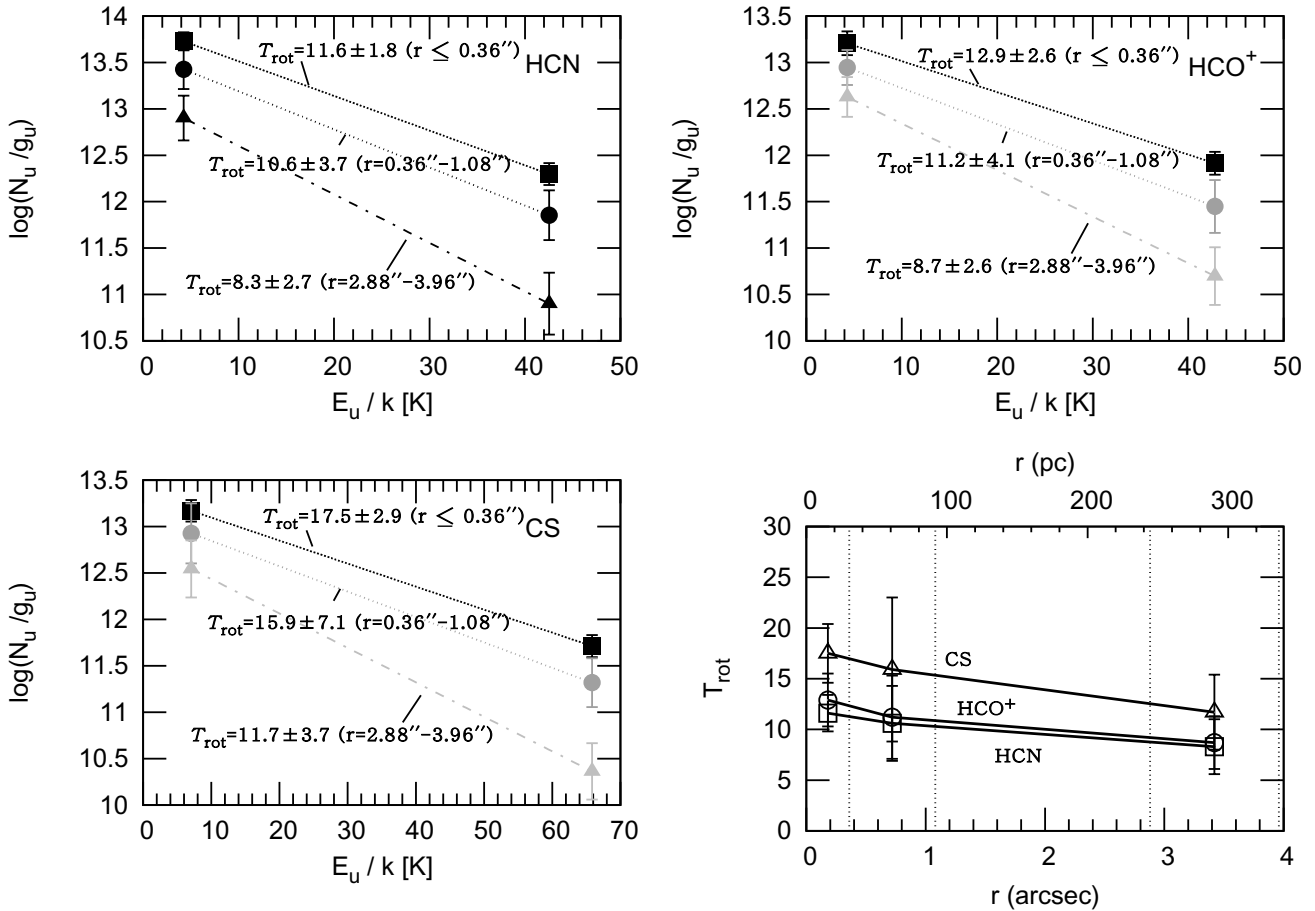
Figure 18 shows the integrated intensity ratio maps of HCN(1–0)/ $\text{HCO}^+(1-0)$ and HCN(1–0)/CS(2–1). We convolved each integrated intensity map to a beam of $0''.72$ and only picked points above a 4σ level in each integrated intensity map. Both the ratios of HCN/ HCO^+ and HCN/CS in the center region are higher than those in the ring, even considering the high ratio at the edge of the ring affected by the low S/N. However, note that the peak of the ratio is offset from the center to the northern west ($r \sim 0''.5 - 0''.6$). The peak position likely corresponds to a region of high velocity dispersion (section 4.4.3 and figure 22).

By dividing the central region of NGC 613 into an annuli with a width of $\Delta r = 0''.72$ from the galactic center ($r \leq 0''.36$), we investigated the variances of HCN(1–0)/ $\text{HCO}^+(1-0)$ and HCN(1–0)/CS(2–1) ratios as a function of the radius. The parameters used to determine the ellipses were $PA = 118^\circ$ and $i = 46^\circ$. The ratios of the integrated intensities were azimuthally averaged in the inner CN ($r \leq 0''.36$), outer CN ($0''.36 \leq r \leq 1''.08$), and star-forming ring ($2''.88 \leq r \leq 3''.96$). The ratio of HCN/ $\text{HCO}^+ = 1.9 \pm 0.1$ at the inner CN decreases gradually with the radius, 1.6 ± 0.2 in the outer CN and 1.3 ± 0.4 in the ring. Similarly, HCN/CS shows radial decrease, 4.6 ± 0.5 in the inner CN, 4.1 ± 1.5 in the outer CN, and 2.9 ± 0.7 in the ring. It is expected that the optical depths of these lines are high ($\tau \gtrsim 1$; e.g., Jiménez-Donaire et al. 2017), as supported by the dips of the spectra at the center (figure 6). For the optically thick case, as the critical density is lower than its nominal value by a factor equal to the optical depth (Shirley 2015, Jiménez-Donaire et al. 2017), these lines can be thermalized. Under these conditions, the intensity ratios mainly depend on the abundance ratio. Actually, the variations of the abundance ratios of $N(\text{HCN})/N(\text{HCO}^+)$ and $N(\text{HCN})/N(\text{CS})$ from the inner CN to the ring (table 17) can be found to correspond to the variation of the intensity ratios.

For Band 7 data, we divided the central region of NGC 613 into annuli with widths of $\Delta r = 0''.36$ from the center ($r \leq 0''.18$). The integrated intensities were convolved to a beam of $0''.36$. In a manner similar to Band 3, the ratios of the integrated intensities were azimuthally averaged in the inner CN, outer CN, star-forming ring, and the intermediate region between the CN and ring (the inter-ring; $1''.08 \leq r \leq 2''.88$). Figure 19(a) shows the variances of the HCN(4–3)/ $\text{HCO}^+(4-3)$ and HCN(4–3)/CS(7–6) ratios as a function of the radius. The

Table 4. Resultant parameters from rotational diagrams.

	Inner CND	Outer CND	Star forming ring
T_{rot} (HCN) [K]	11.6 ± 1.8	10.6 ± 3.7	8.3 ± 2.7
T_{rot} (HCO ⁺) [K]	12.9 ± 2.6	11.2 ± 4.1	8.7 ± 2.6
T_{rot} (CS) [K]	17.5 ± 2.9	15.9 ± 7.1	11.7 ± 3.7
$N(\text{HCN}) [\times 10^{13} \text{cm}^{-2}]$	7.7 ± 0.9	4.0 ± 1.1	1.3 ± 0.4
$N(\text{HCO}^+) [\times 10^{13} \text{cm}^{-2}]$	2.2 ± 0.3	1.3 ± 0.3	0.7 ± 0.2
$N(\text{CS}) [\times 10^{13} \text{cm}^{-2}]$	2.2 ± 0.3	1.3 ± 0.5	0.6 ± 0.2
$N(\text{HCN})/N(\text{HCO}^+)$	3.5 ± 0.7	3.1 ± 1.1	1.9 ± 0.8
$N(\text{HCN})/N(\text{CS})$	3.5 ± 0.7	3.1 ± 1.5	2.2 ± 1.1


Fig. 17. Rotational diagrams of the HCN (top left), HCO⁺ (top right), and CS (bottom left) measurements, and the radial variation of the resultant rotational temperature of the molecules (bottom right). In each rotational diagram, the squares, circles, and triangles present the region of the inner-CND, outer-CND, and star-forming ring, respectively.

ratios of both HCN/HCO⁺ and HCN/CS in the CND decrease gradually with the radius, as is the case in Band 3. We plotted the HCN(4–3)/HCO⁺(4–3) and HCN(4–3)/CS(7–6) ratios in each region on the submillimeter-HCN diagram developed by Izumi et al. (2016) [figure 19(b)]. From the inner CND through outer CND, the HCN(4–3)/CS(7–6) ratio slightly decreases in spite of the constant ratio of HCN(4–3)/HCO⁺(4–3). The ratios of HCN(4–3)/HCO⁺(4–3) and HCN(4–3)/CS(7–6) in the outer CND and inter-ring locate at the border between the AGN and starburst regimes, and the ratios in the star-forming ring are consistent with those of starburst galaxies. The relatively

low HCN/HCO⁺ in the ring could be caused by the HCO⁺ enhancement because HCO⁺ is abundant in strong UV fields, i.e., massive star formation (e.g., Bayet et al. 2011; Meijerink et al. 2011). By adopting the column densities of CS and HCN derived in section 4.1 and a line width of $\sim 200 \text{ km s}^{-1}$ (figure 11), we estimated the ratio of line-of-sight molecular column density to the velocity width as $N_{\text{CS}}/dV (\approx N_{\text{HCN}}/dV) \sim 2 \times 10^{11} (\text{cm}^{-2} \text{ km s}^{-1})$. Under these conditions, it is expected that both CS(7–6) and HCO⁺ are optically thin ($\tau \ll 1$), and the variations of the integrated intensity ratios of HCN(4–3)/CS(7–6) and HCN(4–3)/HCO⁺(4–3) in the regions depend

on the kinetic temperature T_k , volume density of H_2 n_{H_2} and abundance ratio of CS and HCO^+ relative to HCN (Izumi et al. 2016).

4.3 Non-LTE analysis of HCN, HCO^+ , and CS

We investigated the difference of the physical parameters (T_{kin} , n_{H_2} , and N_{H_2}) in the CND ($r \lesssim 0''.36$) and ring ($2''.88 \lesssim r \lesssim 3''.96$) by utilizing the intensity ratios of HCN, HCO^+ , and CS through the non-LTE radiative transfer code RADEX (van der Tak et al. 2007). RADEX uses an escape probability approximation to solve the non-LTE excitation, assuming that all lines radiate from the same region. We adopted a uniform spherical geometry ($dV = 15 \text{ km s}^{-1}$) and evaluated the minimum residuals between the observed line and modeled intensity ratios. Intensity ratio is described as $R_{J_u J_1 / J'_u J'_1}^{mol} = I_{J_u J_1}^{mol} / I_{J'_u J'_1}^{mol}$, where J_u and J_1 are the upper and lower rotational transitions and $I_{J_u J_1}^{mol}$ is the integrated intensity of a given molecule at transition ($J_u \rightarrow J_1$), as shown by Krips et al. (2008). In our analysis, we convolved the individual integrated intensity maps with a resolution of $0''.72$, and used the averaged intensity ratios of $R_{43/10}^{HCN} = 0.44 \pm 0.07$, $R_{43/43}^{HCN/HCO^+} = 1.41 \pm 0.24$, and $R_{43/76}^{HCN/CS} = 5.70 \pm 0.97$ at the CND, and $R_{43/10}^{HCN} = 0.10 \pm 0.05$, $R_{43/43}^{HCN/HCO^+} = 0.75 \pm 0.44$, and $R_{43/76}^{HCN/CS} = 4.62 \pm 2.60$ in the ring. All line specifications (spectroscopic data and collisional excitation rates) were taken from the Leiden Atomic and Molecular Database (LAMDA: Schöier et al. 2005). For our non-LTE analysis, we varied the gas kinetic temperature within a range of $T_k = 10\text{--}700 \text{ K}$ with steps of $\Delta T_k = 10 \text{ K}$, the H_2 column density of $N_{H_2} = 10^{18}\text{--}10^{25} \text{ cm}^{-2}$ with steps of $\Delta N_{H_2} = 10^{1.0} \text{ cm}^{-2}$, and gas density of $n_{H_2} = 10^3\text{--}10^9 \text{ cm}^{-3}$ with steps of $\Delta n_{H_2} = 10^{0.25} \text{ cm}^{-3}$. Our LTE analysis shows the comparable abundance of HCO^+ and CS with respect to HCN (table 4); it is compatible with the results in the central region of NGC 1097 (Martín et al. 2015), and hence we assumed that the relative abundance ratios $[HCN]/[HCO^+]$ are the same as $[HCN]/[CS]$. We considerably changed the initial parameters of the relative abundance ratios, $[HCN]/[CS]$ and $[HCN]/[HCO^+]$ to 1, 5, 10, 20, 30, 40, and 50, where $[HCO^+]/[H_2] = 1.0 \times 10^{-9}, 5.0 \times 10^{-9}$ (e.g., Paglione et al. 1995, Martín et al. 2006), and the background temperature $T_{bg} = 2.7, 10, 20, 30, 40, 50 \text{ K}$.

Under these conditions, we applied RADEX and conducted a χ^2 test, that is, $\chi^2 = \{[R_{J_u J_1 / J'_u J'_1}^{mol}(\text{obs}) - R_{J_u J_1 / J'_u J'_1}^{mol}(\text{model})] / \sigma R_{J_u J_1 / J'_u J'_1}^{mol}(\text{obs})\}^2$, where $\sigma R_{J_u J_1 / J'_u J'_1}^{mol}(\text{obs})$ is the standard deviation of the observed intensity ratio to search for the best parameters to explain the observed intensities. We confirmed that reasonable solutions based on the χ^2 test could not be obtained when $T_{bg} \geq 10 \text{ K}$. Figures 20(a) and (b) show the resultant best-fitted parameters in the CND and ring, respectively. The dashed

lines in figure 20 are the $\pm 1\sigma$ error of each ratio, and the dark regions indicate the regions where $\chi^2 < 1$. The best-fitted parameters with $\chi^2 \lesssim 1$ at the CND were obtained to be $T_k = 350\text{--}550 \text{ K}$, $n_{H_2} \sim 10^{4.5} \text{ cm}^{-3}$, and $N_{H_2} = 10^{22} \text{ cm}^{-2}$ when $[HCN]/[HCO^+] = 10$ and $[HCN]/[CS] = 10$. In the ring, the best-fitted parameters with $\chi^2 \lesssim 1$ were $T_k = 80\text{--}300 \text{ K}$, $n_{H_2} \sim 10^{4.5\text{--}5} \text{ cm}^{-3}$, and $N_{H_2} = 10^{22} \text{ cm}^{-2}$ when $[HCN]/[HCO^+] = 10$ and $[HCN]/[CS] = 10$. The derived column densities are comparable to that derived from the CO(3–2) flux: $N_{H_2} = 0.9 \times 10^{22} \text{ cm}^{-2}$. The discrepancy in the abundance ratios of HCO^+ and CS with respect to HCN between the LTE analysis ($[HCN]/[HCO^+] \approx [HCN]/[CS] \sim 3$) and non-LTE analysis ($[HCN]/[HCO^+] = [HCN]/[CS] = 10$) can be caused by the subthermal emission for high transition lines, i.e., the density $n_{H_2} \sim 10^{4\text{--}4.5} \text{ cm}^{-3}$ is not high enough to thermalize these lines ($n_{H_2}^{crit} \sim 10^{6\text{--}7} \text{ cm}^{-3}$). Therefore, the high abundance ratios $[HCN]/[HCO^+]$ and $[HCN]/[CS]$ are needed to satisfy the observed line ratios. In addition, NGC 1097, which shows the similar discrepancy between the abundance ratio estimated through LTE and non-LTE analyses, has been reported (Martín et al. 2015, Izumi et al. 2016). By adopting the intensity ratios based on HCO^+ , i.e., $R_{43/10}^{HCO^+} = 0.60 \pm 0.10$ (CND) and 0.15 ± 0.06 (ring), $R_{43/43}^{HCO^+/HCN} = 0.71 \pm 0.12$ (CND) and 1.33 ± 0.78 (ring), and $R_{43/76}^{HCO^+/CS} = 4.04 \pm 0.70$ (CND) and 6.26 ± 3.20 (ring), in the analysis, we derived the best-fitted parameters $T_k \sim 300\text{--}400 \text{ K}$, $n_{H_2} \sim 10^{4.5\text{--}5} \text{ cm}^{-3}$, and $N_{H_2} = 10^{22} \text{ cm}^{-2}$ in the CND and $T_k \sim 100\text{--}300 \text{ K}$, $n_{H_2} \sim 10^{4\text{--}4.5} \text{ cm}^{-3}$, and $N_{H_2} = 10^{22} \text{ cm}^{-2}$ in the ring; these are consistent with the previous results based on HCN. Although the parameters in the ring could not be determined rigidly because of low S/N of the ratios, the kinematic temperature in the CND ($> 300 \text{ K}$) was clearly higher than that in the ring ($\sim 80\text{--}300 \text{ K}$). In addition, these results suggest that the variations of intensity ratios HCN/HCO^+ and HCN/CS in the CND and ring (section 4.2) mainly depend on the kinetic temperature rather than on n_{H_2} and on the enhancement of the abundance ratio of HCO^+ and CS relative to HCN.

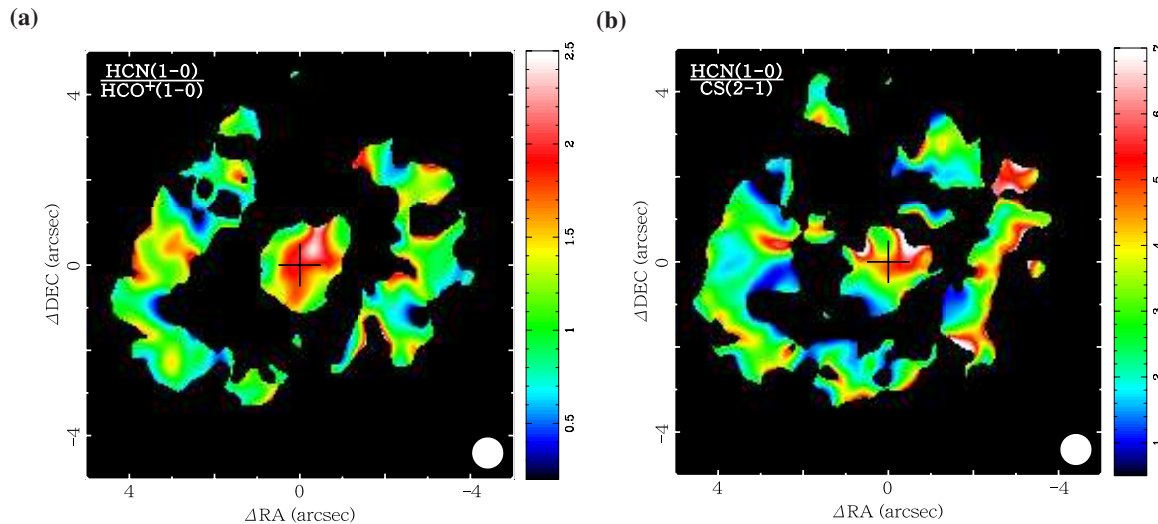


Fig. 18. Integrated intensity ratios of (a) HCN(1–0)-to-HCO⁺(1–0) and (b) HCN(1–0)-to-CS(2–1). The individual intensity maps are convolved with a beam of 0.''72, and values only above 4 σ in the individual maps have been used.

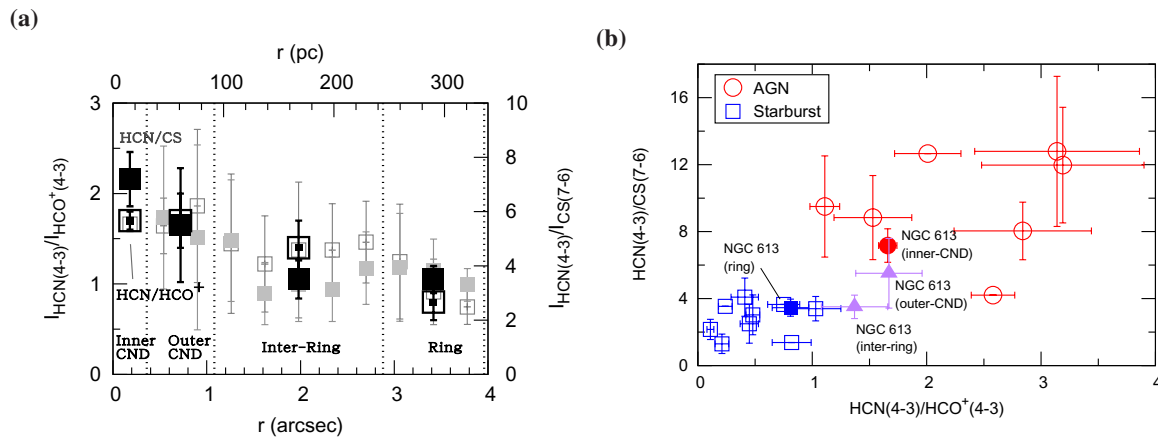


Fig. 19. (a) The ratios of the integrated intensities of HCN/HCO⁺ (open gray square) and HCN/CS (filled gray square) in annuli with a width of $\Delta r = 0.''36$. Open and filled black squares represent azimuthal averages of the integrated intensity ratios of HCN/HCO⁺ and HCN/CS, respectively, in the inner CND ($r \leq 0.''36$), outer CND ($0.''36 \leq r \leq 1.''08$), star-forming ring ($2.''88 \leq r \leq 3.''96$), and inter-ring ($1.''08 \leq r \leq 2.''88$). Vertical dot lines correspond to $r = 0.''36, 1.''08, 2.''88$ and $3.''96$. (b) Diagram of HCN(4–3)/HCO⁺(4–3) and HCN(4–3)/CS(7–6) integrated intensity ratios. The open circles and squares indicate AGNs and starburst galaxies shown in figure 1 of Izumi et al. (2016). The filled circles and squares show the ratios in the inner-CND and star-forming ring of NGC 613, respectively. The filled triangles represent the ratios in the outer-CND and inter-ring for comparison.

Table 5. Surface densities of molecular gas, star-formation rates (SFR) and star-formation efficiencies (SFE) at the nucleus and the spots in the ring.

Positions	Σ_{H_2} [$M_{\odot} \text{pc}^{-2}$]	SFR [$M_{\odot} \text{yr}^{-1}$]*	SFE [$\times 10^{-8} \text{yr}^{-1}$]
Nucleus (CND)	5.1×10^2	0.02	0.7
Spot 1	2.0×10^2	0.03	2.7
Spot 2	1.0×10^2	0.04	7.1
Spot 3	2.1×10^2	0.13	10.9
Spot 4	2.1×10^2	0.10	8.4
Spot 5	1.2×10^2	0.10	14.7
Spot 6	1.6×10^2	0.08	8.8
Spot 7	1.8×10^2	0.06	5.9

* Falc3n-Barroso et al. (2014)

Table 6. Fitted parameters of gas in the north side of the CND

Positions	Component	$F_{\text{CO}32}$ (mJy)	Velocity (km s^{-1})	Δv_{FWHM} (km s^{-1})	$S_{\text{CO}32}$ (Jy km s^{-1})	M_{H_2} ($10^4 M_{\odot}$)*
N ($0''$, $0''5$)	Blue	38.6 ± 2.5	1390.2 ± 0.8	39.8 ± 2.4	1.6 ± 0.1	5.5 ± 0.5
	Wide	23.7 ± 4.8	1468.5 ± 4.4	224.8 ± 20.2	5.7 ± 1.3	19.1 ± 4.2
	Narrow	112.7 ± 4.5	1482.1 ± 0.4	76.8 ± 2.1	9.2 ± 0.4	31.0 ± 1.5
N ($0''$, $0''75$)	Blue	26.0 ± 1.6	1401.7 ± 0.9	37.2 ± 2.9	1.0 ± 0.1	3.5 ± 0.3
	Wide	34.6 ± 1.7	1467.5 ± 2.3	163.6 ± 4.3	6.0 ± 0.3	20.3 ± 1.1
	Narrow	16.7 ± 1.8	1474.2 ± 1.2	31.0 ± 4.3	0.6 ± 0.1	1.9 ± 0.3
NW ($-0''5$, $0''5$)	Red	86.5 ± 8.5	1526.5 ± 3.7	53.0 ± 4.7	4.9 ± 0.6	16.4 ± 2.2
	Wide	35.4 ± 3.1	1477.1 ± 3.4	169.9 ± 7.1	6.4 ± 0.6	21.6 ± 2.1
	Narrow	54.2 ± 11.3	1483.8 ± 5.3	50.2 ± 6.2	2.9 ± 0.7	9.8 ± 2.4
NW ($-0''5$, $0''75$)	Red	33.5 ± 2.1	1528.5 ± 2.7	73.8 ± 7.7	2.6 ± 0.3	8.9 ± 1.1
	Wide	24.9 ± 1.7	1470.9 ± 5.8	193.8 ± 7.6	5.1 ± 0.4	17.3 ± 1.4
	Narrow	28.6 ± 3.2	1479.6 ± 1.0	28.9 ± 3.1	0.9 ± 0.1	3.0 ± 0.5

* Molecular gas mass is derived from equation (1).

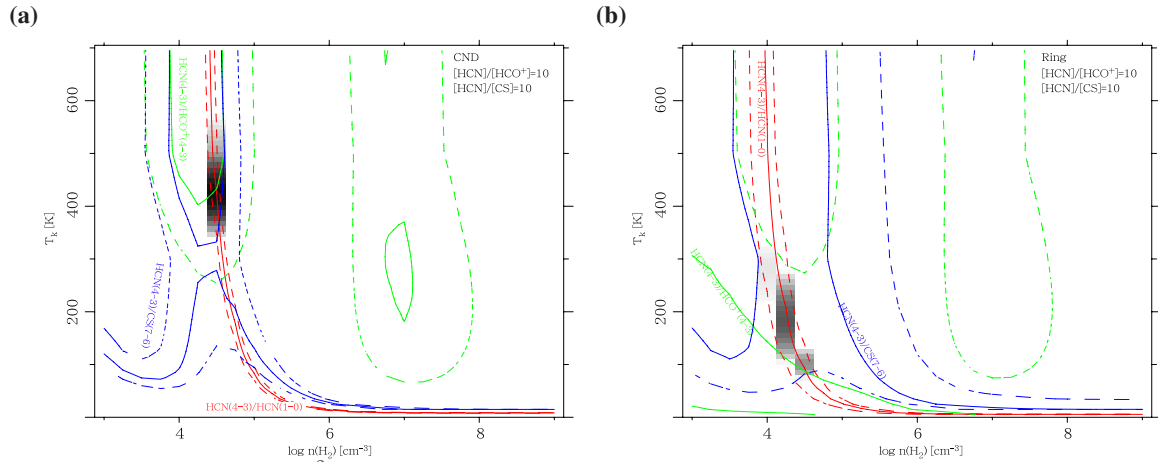


Fig. 20. Representative results of the χ^2 test with RADEX to search for the best parameter sets to explain the observed ratios of HCN(4–3)/HCN(1–0) (red), HCN(4–3)/HCO⁺(4–3) (green), and HCN(4–3)/CS(7–6) (blue) in (a) the CND and (b) the star forming ring. The parameters of the molecular hydrogen column density of $N_{\text{H}_2} = 10^{22} \text{cm}^{-2}$, abundance ratios of HCO⁺ and CS to H₂ [HCO^+/H_2] (and [CS/H_2]) = 5.0×10^{-9} , and abundance ratios of HCN to HCO⁺ and CS [HCN/HCO^+] (and [HCN/CS]) = 10 were adopted both in the CND and ring. The dashed lines are the 1σ error of each track. The background gray scale indicates the value of $\chi^2 < 1$. The best-fitted parameters achieved using these three tracks are $(n_{\text{H}_2}, T_{\text{kin}}) = (\sim 10^{4.5} \text{cm}^{-3}, 350\text{--}550 \text{K})$ at the CND and $(n_{\text{H}_2}, T_{\text{kin}}) = (\sim 10^{4-4.5} \text{cm}^{-3}, 80\text{--}300 \text{K})$ in the star-forming ring.

4.4 Activity of the central region of NGC 613

4.4.1 Low star-formation efficiency at CNL

We found abundant gas in the CNL relative to the ring, while Falc3n-Barroso et al. (2014) showed lower star-formation rate (SFR) in the CNL, $0.02 M_{\odot} \text{ yr}^{-1}$, than those at the spots in the ring, $0.03\text{--}0.13 M_{\odot} \text{ yr}^{-1}$, by using Br γ with SINFONI on the Very Large Telescope. Figure 21 shows that in the CNL, the molecular line intensities are strong, but the Br γ intensity is rather weak, where Br γ is produced through photoionization in the Str3mngren spheres around O- or B-type stars and its intensity is an indicator of SFR. Table 5 shows the star-formation efficiency (SFE) defined as the ratio of the SFR surface density to the surface mass density of molecular hydrogen at each position, where $R_{32/10} = 2$ is adopted. The SFE in the CNL is almost an order of magnitude lower than those at the spots in the star-forming ring. By applying $R_{32/10} = 0.25$ in the ring because $R_{32/10}$ decreases with radius (section 3.3.2), the difference in the SFEs between the CNL and ring is increased further. The weak intensity of C $_2$ H, which is a tracer of massive star formation, also indicates inactive star formation in the CNL (section 3.2.1).

The much lower SFE in the CNL cannot be caused by the underestimation of the SFR or uncertainty of the estimated surface density of molecular gas. Br γ is affected by dust extinction, although lesser than H α . Falc3n-Barroso et al. (2014) determined the amount of extinction at the spots in the ring from the Brackett decrement Br γ /Br10 to be the visual extinction of $A_V = 6.50\text{--}15.27$ at the spots. In contrast, the extinction at the CNL $A_V = 3.62$ was estimated using the color excess $E(H - K)$ and CO line strength index due to the low S/N of the Br lines. Even if the difference of the two measurements is considered, generally 2–5, the SFE at the CNL remains lower than those at the spots. The uncertainty of the surface density of molecular gas is mainly caused by $R_{32/10}$ and $X_{\text{CO}} = N(\text{H}_2)/I_{\text{CO}}$. $R_{32/10} (= 2)$ may be overestimated in the ring and $X_{\text{CO}} [= 0.5 \times 10^{20} \text{ cm}^{-2} (\text{K km s}^{-1})^{-1}]$ is expected to increase with the radius (e.g., Nakai & Kuno 1995, Bolatto et al. 2013). Given that $R_{32/10}$ in the CNL is four times higher than that in the ring (e.g., Tsai et al. 2012) and X_{CO} in the center is ~ 0.3 dex lower than that in the galactic disk (e.g., Sandstrom et al. 2013), SFEs in the CNL and the spots change from the values in table 5 to $7.8 \times 10^{-5} \text{ yr}^{-1}$ and $1.2 \pm 0.5 \times 10^{-4} \text{ yr}^{-1}$, respectively. SFE at the CNL is still lower than those at the spots.

4.4.2 Heating source of molecular gas in CNL

We determined that the temperature of the molecular gas in the CNL ($T_{\text{rot}} \sim 12 \text{ K}$, $T_{\text{k}} > 300 \text{ K}$) is higher than that in the ring ($T_{\text{rot}} \sim 8 \text{ K}$, $T_{\text{k}} \sim 80\text{--}300 \text{ K}$), and the ratios of the HCN(4–3)/HCO $^+$ (4–3) and HCN(4–3)/CS(7–6) in the CNL locate at the AGN domain (figure 19) except the starburst. In addition to

the findings that Br γ emission in the CNL is weaker than that in the ring (Falc3n-Barroso et al. 2014), Asmus et al. (2014) demonstrated that the nuclear MIR flux of NGC 613 is considerably lower ($\sim 6\%$) than that in the ring, marginally resolving the nucleus with T-ReCS in the N-filter mounted on Gemini-South ($\theta_{\text{FWHM}} \sim 0''.39$). These results indicate that the star-formation activity is an unlikely dominant heating source for the hot gas in the CNL.

Goulding & Alexander (2009) identified that NGC 613 hosts AGN, based on the detection of an emission line [Ne V] $\lambda 14.32 \mu\text{m}$ by using *Spitzer*/IRS ($4''.7 \times 11''.3$ for $\lambda \sim 9.9\text{--}19.6 \mu\text{m}$). However, by using the ratios among emission lines, e.g., [Ne V], [Ne II], and [O III], and IR luminosity, they suggested that the activity of the central region of NGC 613 is dominated by star formation (AGN contribution $< 5\%$). Falc3n-Barroso et al. (2014) discussed about the heating source of molecular gas at the CNL, and concluded that the gas cannot be excited through photoionization by UV and soft X-ray radiation but through shock by the nuclear jets, by comparing the flux ratios of [Fe II]/Br γ , H $_2$ (1–0) S(1)/H $_2$ (2–1) S(1), and H $_2$ (1–0) S(2)/H $_2$ (1–0) S(0) in the CNL with those in the ring and theoretical model. The distribution of the steep spectral index derived from 4.9 and 95 GHz around the center ($\alpha \lesssim -0.6$, figure 2) and the feature of outflowing gas around the CNL in the PV-diagram (figure 13) are compatible with the mechanical heading by the jets.

4.4.3 Outflow of molecular gas in CNL

Figures 22 (a) and (b) show maps of the intensity-weighted CO velocity field ($\bar{v} = \sum(Tv)/\sum T$) and intensity-weighted CO velocity dispersion ($\Delta v = \sqrt{\sum[T(v - \bar{v})^2]/\sum T}$), where T is the intensity per channel. The velocity dispersion at the west-side of the ring ($\Delta v \approx 50 \text{ km s}^{-1}$) is comparable to that in the CNL because the velocity components along the galactic bar are overlapped in the beam and the dispersion may be overestimated because the baseline range in a spectrum is not enough for high velocity (section 2). The northern CNL shows high velocity dispersion ($\Delta v \gtrsim 50 \text{ km s}^{-1}$) in agreement with that of [Fe II] (B3ker et al. 2008, Falc3n-Barroso et al. 2014); however their distribution is different, i.e., $\theta_{\text{PA}} \sim -20^\circ$ for CO and $\theta_{\text{PA}} \sim 30^\circ$ for [Fe II]. In addition, the large dispersion extends towards north-west and north-east [figure 22(d)] regardless of the distribution of molecular gas [figure 22(c)]. Figure 22(e) shows the representative spectra in the north and northwest regions of the CNL. The spectra are fitted by three Gaussians, and the resultant parameters are summarized in table 6. In addition to the broad emission features of $\Delta v_{\text{FWHM}} > 150 \text{ km s}^{-1}$ and narrow features of $\Delta v_{\text{FWHM}} \sim 30\text{--}80 \text{ km s}^{-1}$ close to the rotational and systemic velocities, which probably reflect the gas in the disk, the blueshifted and redshifted features are clearly decomposed in the north and northwest regions, respectively.

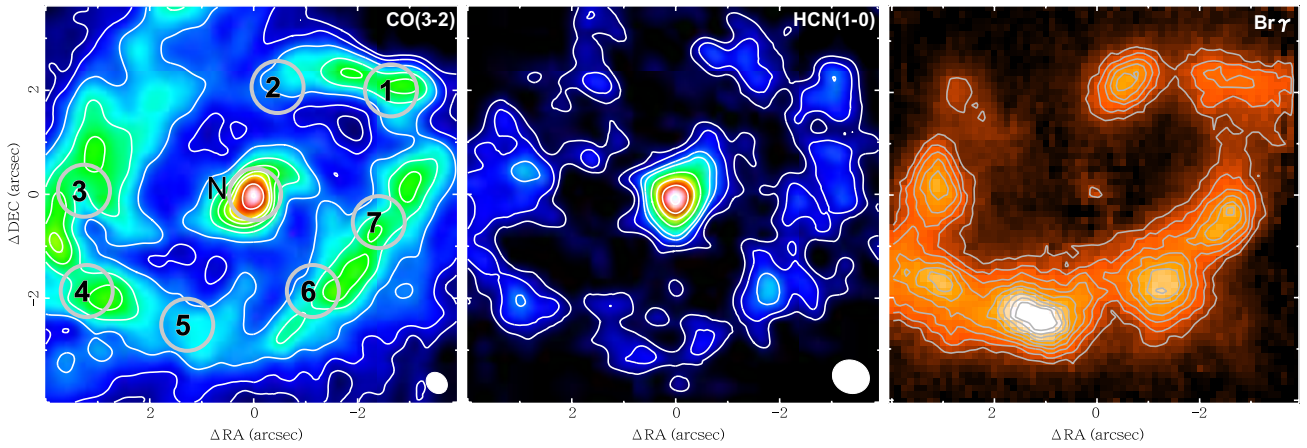


Fig. 21. Enlarged integrated intensity maps of our (a) CO(3–2) and (b) HCN(1–0) to match (c) Br γ image with VLT (Falcón–Barroso et al. 2014). The circles mark the positions of the nucleus and spots 1 through 7 denoted by Falcón–Barroso et al. (2014).

The molecular gas mass of each component is estimated to be of $\sim 10^5 M_{\odot}$ (table 6). We calculated the virial mass given by $M_{\text{vir}} = 1040 \sigma_v R$, where σ_v is the cloud velocity dispersion in km s^{-1} and R is the cloud radius in pc (Solomon et al. 1987), assuming a spherical cloud with a density profile $\rho \propto r^{-1}$ and size of ~ 30 pc being comparable with the beam size for simplicity. The virial mass ($\gtrsim 10^6 M_{\odot}$) is obviously larger than the CO luminosity mass, suggesting that the molecular gas is not a gravitationally bound state.

Both the blueshifted and redshifted components may not be coplanar gases because the systematic vertical gas motion to the disk is unlikely. Considering that the northern part of the galactic disk is the far side, the blueshifted and redshifted components are regarded as the outflowing gas from the disk and the gas dragged by the jets in the disk, respectively. The observed distribution and kinematics of the molecular gas could be explained by the effect of the radio jets. The simulations of Wagner & Bicknell (2011) and Wagner et al. (2012) have shown that the jets create a spherical bubble as propagating through ISM and a cocoon of shocked material accelerates molecular gas to high velocities and over a wide range of directions, preventing star formation in the CND, i.e., negative feedback. In the future, we will discuss the relation between molecular gas and the NGC 613 jets in detail. However, to discuss the relation observations of CO(1–0) with higher angular resolution ($\theta_{\text{FWHM}} < 0''.1$) are needed (e.g., Cicone et al. 2012).

5 Summary

In this study, we made observations of molecular lines and continuum emission toward NGC 613 by using ALMA Bands 3 and 7. The main conclusions are summarized as follows:

1. Radio continuum emissions were detected at 95 and 350 GHz from both the CND and star-forming ring. The 95 GHz continuum extends from the center at a position an-

gle of $20^{\circ} \pm 8^{\circ}$. The archival 4.9 GHz data and our 95 GHz data show spectral indices of $\alpha \lesssim -0.6$ and -0.2 along the jet and in the star-forming ring; these can be produced by synchrotron and free-free emissions, respectively.

2. The emission of CO(3–2), HCN(1–0), HCN(4–3), HCO $^{+}$ (1–0), HCO $^{+}$ (4–3), CS(2–1), and CS(7–6) was detected in both the CND and ring. While SiO(2–1) was detected marginally at the edge of the radio jets, C $_2$ H(1–0, 3/2–1/2) was detected unexpectedly in the east side of the ring.
3. The basic parameters of NGC 613 were derived to be the systemic velocity $V_{\text{sys}} = 1471 \pm 3 \text{ km s}^{-1}$, position angle $\theta_{\text{maj}} = 118^{\circ} \pm 4^{\circ}$, and inclination angle $i = 46^{\circ} \pm 1^{\circ}$ in the region $0''.2 \gtrsim r \gtrsim 4''.5$. The velocity field shows rigid rotation as a function of $V_{\text{rot}} = (49 \pm 1) [\text{km s}^{-1} \text{ arcsec}^{-1}] \times r$ at $r > 0''.5$; however, velocity increases steeply in the central region ($r < 0''.5 \approx 42$ pc). Next, a velocity lower than V_{sys} is featured, bridging between the CND and southern part of the ring, and may be a sign of the outflow from the CND.
4. The molecular gas mass in the region $r \leq 5''$ is $M_{\text{H}_2} = 7.2 \times 10^7 - 5.8 \times 10^8 M_{\odot}$ for $R_{32/10} = 0.25 - 2$. The radial distribution of the surface density of the molecular gas Σ_{H_2} derived from CO(3–2) shows an exponential decrease of $\Sigma_{\text{H}_2} = 1330 \exp(-r/r_e) [M_{\odot} \text{ pc}^{-2}]$, where $r_e = 0''.48 (= 41 \text{ pc})$ at $r \leq 100$ pc.
5. The rotational temperatures and column densities of the molecules derived from $J = 1 - 0$ and $4 - 3$ lines of HCN and HCO $^{+}$ and $J = 2 - 1$ and $7 - 6$ of CS in the CND are as follows: $T_{\text{rot}} = 11.6 \pm 1.8 \text{ K}$, $N(\text{HCN}) = 7.7 \pm 0.9 \times 10^{13} [\text{cm}^{-2}]$ for HCN, $T_{\text{rot}} = 12.9 \pm 2.6 \text{ K}$, $N(\text{HCO}^{+}) = 2.2 \pm 0.3 \times 10^{13} [\text{cm}^{-2}]$ for HCO $^{+}$, and $T_{\text{rot}} = 17.5 \pm 2.9 \text{ K}$, $N(\text{CS}) = 2.2 \pm 0.3 \times 10^{13} [\text{cm}^{-2}]$ for CS. The rotational temperature decreased with distance from the center.
6. The variations of the HCN(1–0)/HCO $^{+}$ (1–0) and HCN(1–0)/CS(2–1) ratios from the CND through the ring correspond to the variations of the abundance ratio of HCO $^{+}$ and CS

with respect to HCN. The ratios of HCN(4–3)/HCO⁺(4–3) and HCN(4–3)/CS(7–6) in the CNB and ring are consistent with the ratios in the AGN and starburst domains already reported, respectively. The HCN(4–3)/HCO⁺(4–3) and HCN(4–3)/CS(7–6) ratios likely depend on the kinetic temperature rather than the volume density of H₂ and the abundance ratio of HCO⁺ and CS with respect to HCN.

7. The physical parameters in the inner CNB, utilizing the intensity ratios of HCN, HCO⁺, and CS and assuming non-LTE radiative transfer are $T_k = 350\text{--}550$ K, $n_{H_2} \sim 10^{4.5}$ cm⁻³, and $N_{H_2} = 10^{22}$ cm⁻² with $\chi^2 < 1$ for [HCN]/[HCO⁺] = 10 and [HCN]/[CS] = 10, and $T_k = 80\text{--}300$ K, $n_{H_2} = 10^{4\text{--}4.5}$ cm⁻³, and $N_{H_2} = 10^{22}$ cm⁻² for [HCN]/[HCO⁺] = 10 and [HCN]/[CS] = 10 in the ring. However, the parameters could not be determined rigidly because of the low S/N.
8. The SFE in the CNB is almost an order of magnitude lower than those at the spots in the star-forming ring, even though the dominant activity of the central region is the star formation rather than AGN. The large velocity dispersion of CO extending toward the north side of the CNB and decomposing into blueshifted and redshifted features are probably explained by the effect of the radio jets. These results strongly suggest that the jets heat gas in the CNB where the feedback prevents star formation.

Acknowledgments

We are grateful to the anonymous referee for careful and constructive comments that improved this paper. We thank J. Falcón-Barroso for providing us the data with VLT (figure 15 and 21) and T. Minamidani for useful discussions. This paper makes use of the following ALMA data: ADS/JAO.ALMA#2013.1.01329.S. ALMA is a partnership of ESO (representing its member states), NSF (USA) and NINS (Japan), together with NRC (Canada) and NSC and ASIAA (Taiwan) and KASI (Republic of Korea), in cooperation with the Republic of Chile. The Joint ALMA Observatory is operated by ESO, AUI/NRAO and NAOJ. We referred a script developed by Y. Tamura for this calculation. This research has made use of the NASA/IPAC Extragalactic Database (NED) which is operated by the Jet Propulsion Laboratory, California Institute of Technology, under contract with the National Aeronautics and Space Administration. The National Radio Astronomy Observatory is a facility of the National Science Foundation operated under cooperative agreement by Associated Universities, Inc. Data analysis was in part carried out on the open use data analysis computer system at the Astronomy Data Center, ADC, of the National Astronomical Observatory of Japan.

References

- Aalto, S., Martín, S., Costagliola, F., et al. 2015, *A&A*, 584, A42
- Aladro, R., Martín-Pintado, J., Martín, S., Mauersberger, R., & Bayet, E. 2011, *A&A*, 525, A89
- Asmus, D., Hönig, S. F., Gandhi, P., Smette, A., & Duschl, W. J. 2014, *MNRAS*, 439, 1648
- Bayet, E., Aladro, R., Martín, S., Viti, S., & Martín-Pintado, J. 2009, *ApJ*, 707, 126
- Bayet, E., Williams, D. A., Hartquist, T. W., & Viti, S. 2011, *MNRAS*, 414, 1583
- Beifiori, A., Courteau, S., Corsini, E. M., & Zhu, Y. 2012, *MNRAS*, 419, 2497
- Beuther, H., Semenov, D., Henning, T., & Linz, H. 2008, *ApJL*, 675, L33
- Binney, J., & Tremaine, S. 1987, Princeton, NJ, Princeton University Press, 1987, 747 p.,
- Böker, T., Falcón-Barroso, J., Schinnerer, E., Knapen, J. H. and Ryder, S. 2008, *AJ*, 135, 479
- Bolato, A. D., Wolfire, M., & Leroy, A. K. 2013, *ARA&A*, 51, 207
- Burbidge, E. M., Burbidge, G. R., Rubin, V. C., & Prendergast, K. H. 1964, *ApJ*, 140, 85
- Castangia, P., Panessa, F., Henkel, C., Kadler, M., & Tarchi, A. 2013, *MNRAS*, 436, 3388
- Cicone, C., Feruglio, C., Maiolino, R., et al. 2012, *A&A*, 543, A99
- Combes, F., García-Burillo, S., Casasola, V., et al. 2013, *A&A*, 558, A124
- Condon, J. J. 1992, *ARA&A*, 30, 575
- Davis, B. L., Berrier, J. C., Johns, L., et al. 2014, *ApJ*, 789, 124
- de Vaucouleurs, G., de Vaucouleurs, A., Corwin, H. G., Jr., et al. 1991, Third Reference Catalogue of Bright Galaxies. Volume I: Explanations and references. Volume II: Data for galaxies between 0^h and 12^h. Volume III: Data for galaxies between 12^h and 24^h., by de Vaucouleurs, G.; de Vaucouleurs, A.; Corwin, H. G., Jr.; Buta, R. J.; Paturel, G.; Fouqué, P. Springer, New York, NY (USA), 1991, 2091 p.,
- Di Teodoro, E. M., & Fraternali, F. 2015, *MNRAS*, 451, 3021
- Dumke, M., Nieten, C., Thuma, G., Wielebinski, R., & Walsh, W. 2001, *A&A*, 373, 853
- Elfhag, T., Booth, R. S., Hoeglund, B., Johansson, L. E. B., & Sandqvist, A. 1996, *A&AS*, 115, 439
- Falcón-Barroso, J., Ramos Almeida, C., Bökler, T., Schinnerer, E., Knapen, J. H., Lançon, A. and Ryder, S. 2014, *MNRAS*, 438, 329
- Feldmeier, J. J., Ciardullo, R., & Jacoby, G. H. 1997, *ApJ*, 479, 231
- García-Burillo, S., Combes, F., Usero, A., et al. 2014, *A&A*, 567, A125
- Goulding, A. D., & Alexander, D. M. 2009, *MNRAS*, 398, 1165
- Hollenbach, D., & McKee, C. F. 1989, *ApJ*, 342, 306
- Hummel, E., Jorsater, S., Lindblad, P. O., & Sandqvist, A. 1987, *A&A*, 172, 51
- Hummel, E., & Jorsater, S. 1992, *A&A*, 261, 85
- Hunt, L. K., & Malkan, M. A. 1999, *ApJ*, 516, 660
- Izumi, T., Kohno, K., Martín, S., et al. 2013, *PASJ*, 65,
- Izumi, T., Kohno, K., Aalto, S., et al. 2016, *ApJ*, 818, 42
- Jiménez-Donaire, M. J., Bigiel, F., Leroy, A. K., et al. 2017, *MNRAS*, 466, 49
- Kohno, K., Tosaki, T., Matsushita, S., et al. 2002, *PASJ*, 54, 541
- Koribalski, B. S., Staveley-Smith, L., Kilborn, V. A., et al. 2004, *AJ*, 128, 16
- Krips, M., Neri, R., García-Burillo, S., et al. 2008, *ApJ*, 677, 262-275
- Krips, M., Martín, S., Eckart, A., et al. 2011, *ApJ*, 736, 37
- Lin, M.-Y., Davies, R. I., Burtscher, L., et al. 2016, *MNRAS*, 458, 1375
- Liu, J.-F., & Bregman, J. N. 2005, *ApJS*, 157, 59
- Maloney, P. R., Hollenbach, D. J., & Tielens, A. G. G. M. 1996, *ApJ*, 466, 561
- Mao, R.-Q., Schulz, A., Henkel, C., et al. 2010, *ApJ*, 724, 1336
- Mauersberger, R., Henkel, C., Walsh, W., & Schulz, A. 1999, *A&A*, 341, 256

- Martín, S., Mauersberger, R., Martín-Pintado, J., Henkel, C., & García-Burillo, S. 2006, *ApJS*, 164, 450
- Martín, S., Kohno, K., Izumi, T., et al. 2015, *A&A*, 573, A116
- Martín, S., Aalto, S., Sakamoto, K., et al. 2016, *A&A*, 590, A25
- Martín-Pintado, J., Bachiller, R., & Fuente, A. 1992, *A&A*, 254, 315
- Matsushita, S., Sakamoto, K., Kuo, C.-Y., et al. 2004, *ApJL*, 616, L55
- Meier, D. S., & Turner, J. L. 2005, *ApJ*, 618, 259
- Meijerink, R., & Spaans, M. 2005, *A&A*, 436, 397
- Meijerink, R., Spaans, M., Loenen, A. F., & van der Werf, P. P. 2011, *A&A*, 525, A119
- McMullin, J. P., Waters, B., Schiebel, D., Young, W., & Golap, K., 2007, *Astronomical Data Analysis Software and Systems XVI*, 376, 127
- Muraoka, K., Kohno, K., Tosaki, T., et al. 2007, *PASJ*, 59, 43
- Nakai, N., & Kuno, N. 1995, *PASJ*, 47, 761
- Nishiyama, K., Nakai, N., & Kuno, N. 2001, *PASJ*, 53, 757
- Paglione, T. A. D., Jackson, J. M., Ishizuki, S., & Rieu, N.-Q. 1995, *AJ*, 109, 1716
- Regan, M. W., & Teuben, P. J. 2004, *ApJ*, 600, 595
- Sakamoto, K., Okumura, S. K., Ishizuki, S., & Scoville, N. Z. 1999, *ApJ*, 525, 691
- Sanders, D. B., Mazzarella, J. M., Kim, D.-C., Surace, J. A., & Soifer, B. T. 2003, *AJ*, 126, 1607
- Sandstrom, K. M., Leroy, A. K., Walter, F., et al. 2013, *ApJ*, 777, 5
- Schöier, F. L., van der Tak, F. F. S., van Dishoeck, E. F., & Black, J. H. 2005, *A&A*, 432, 369
- Scoville, N., Sheth, K., Walter, F., et al. 2015, *ApJ*, 800, 70
- Sheth, K., Vogel, S. N., Regan, M. W., Thornley, M. D., & Teuben, P. J. 2005, *ApJ*, 632, 217
- Sheth, K., Regan, M., Hinz, J. L., et al. 2010, *PASP*, 122, 1397
- Shirley, Y. L. 2015, *PASP*, 127, 299
- Skrutskie, M. F., Cutri, R. M., Stiening, R., Weinberg, M. D., Schneider, S., Carpenter, J. M., Beichman, C., Capps, R., Chester, T., Elias, J., Huchra, J., Liebert, J., Lonsdale, C., Monet, D. G., Price, S., Seitzer, P., Jarrett, T., Kirkpatrick, J. D., Gizis, J. E., Howard, E., Evans, T., Fowler, J., Fullmer, L., Hurt, R., Light, R., Kopan, E. L., Marsh, K. A., McCallon, H. L., Tam, R., Van Dyk, S., Wheelock, S. 2006, *AJ*, 131, 1163
- Solomon, P. M., Rivolo, A. R., Barrett, J., & Yahil, A. 1987, *ApJ*, 319, 730
- Tsai, M., Hwang, C.-Y., Matsushita, S., Baker, A. J., & Espada, D. 2012, *ApJ*, 746, 129
- Tully, R. B. 1988, Cambridge and New York, Cambridge University Press, 1988, 221 p.,
- van der Tak, F. F. S., Black, J. H., Schöier, F. L., Jansen, D. J., & van Dishoeck, E. F. 2007, *A&A*, 468, 627
- Viti, S., García-Burillo, S., Fuente, A., et al. 2014, *A&A*, 570, A28
- Vlahakis, C., van der Werf, P., Israel, F. P., & Tilanus, R. P. J. 2013, *MNRAS*, 433, 1837
- Wada, K. 2012, *ApJ*, 758, 66
- Wagner, A. Y., & Bicknell, G. V. 2011, *ApJ*, 728, 29
- Wagner, A. Y., Bicknell, G. V., & Umemura, M. 2012, *ApJ*, 757, 136
- Young, J. S., Xie, S., Tacconi, L., et al. 1995, *ApJS*, 98, 219

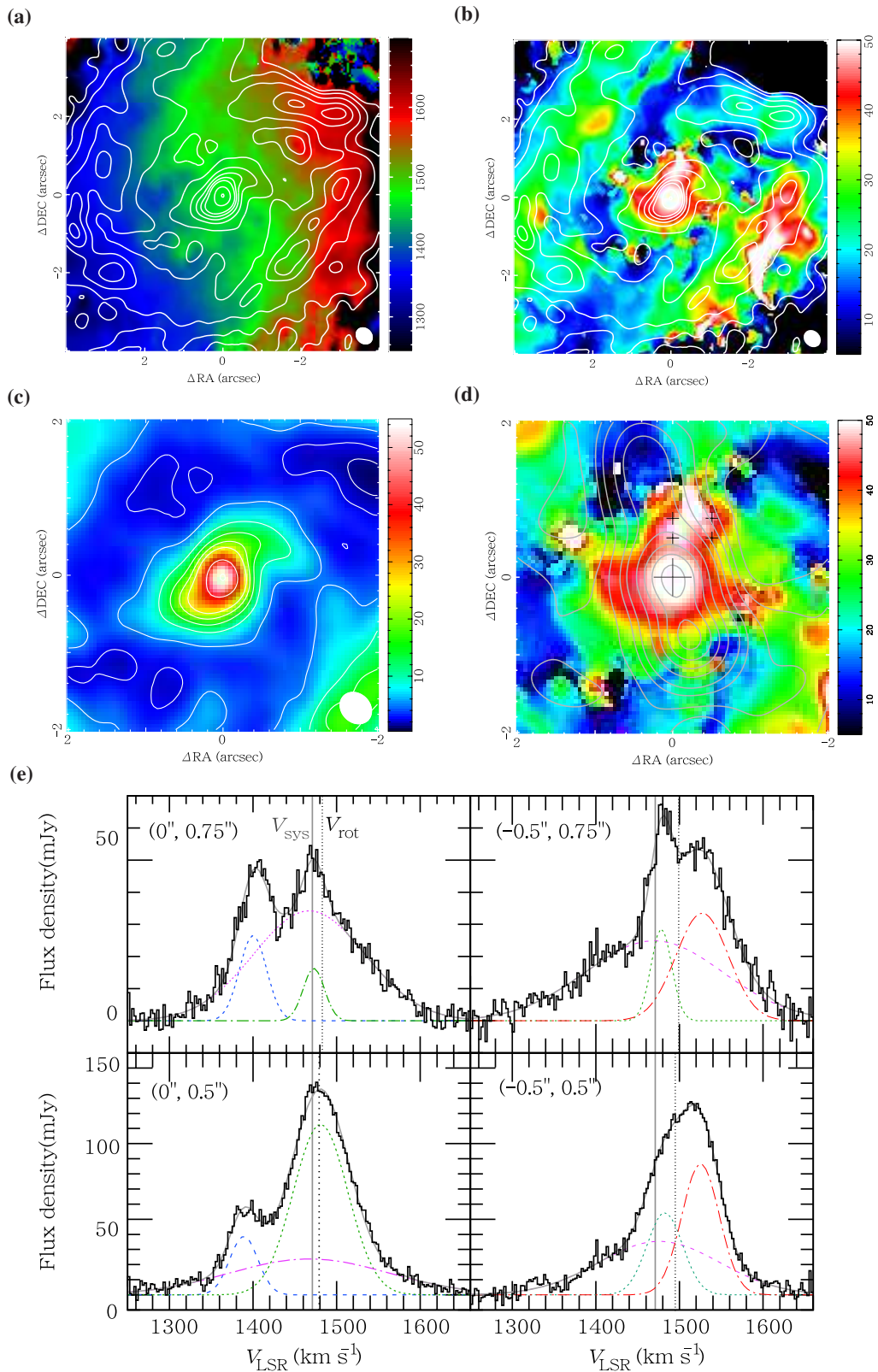


Fig. 22. (a) CO(3–2) velocity field map derived from intensity-weighted mean velocities. (b) Intensity-weighted CO velocity dispersion map. Enlarged view of (c) the integrated intensity maps of CO(3–2) and (d) intensity-weighted CO velocity dispersion map. The contours in (d) are same as the 4.9 GHz continuum map presented in figure 2. (e) Representative CO(3–2) spectra in the north side, $(\Delta RA, \Delta DEC) = (0'', 0''.75)$ and $(0'', 0''.5)$, and the northwest side, $(-0''.5, 0''.75)$ and $(-0''.5, 0''.5)$. The positions are shown in (d). The three Gaussian fits to the lines are overlaid with dotted lines.